The Design and Realization of a Sensitive Walking Platform

by

Vadim Chernyak

A Thesis

Submitted to the Faculty

of the

WORCESTER POLYTECHNIC INSTITUTE

in partial fulfillment of the requirements for the

Degree of Master of Science

in

Mechanical Engineering

by

_____

April 18, 2012

APPROVED:

_____

Dr. Stephen S. Nestinger, Co-Advisor

_____

Dr. Eduardo Torres-Jara, Co-Advisor

_____

Dr. Gregory Fischer, Thesis Committee Member

_____

Dr. John M. Sullivan, Thesis Committee Member

_____

Dr. Simon W. Evans, Graduate Committee Representative

Abstract

Legged locomotion provides robots with the capability of adapting to different terrain conditions. General complex terrain traversal methodologies solely rely on proprioception which readily leads to instability under dynamical situations. Biological legged locomotion utilizes somatosensory feedback to sense the real-time interaction of the feet with ground to enhance stability. Nevertheless, limited attention has been given to sensing the feet-terrain interaction in robotics. This project introduces a paradigm shift in robotic walking called sensitive walking realized through the development of a compliant bipedal platform. Sensitive walking extends upon the success of sensitive manipulation which utilizes tactile feedback to localize an object to grasp, determine an appropriate manipulation configuration, and constantly adapts to maintain grasp stability. Based on the same concepts of sensitive manipulation, sensitive walking utilizes podotactile feedback to enhance real-time walking stability by effectively adapting to variations in the terrain. Adapting legged robotic platforms to sensitive walking is not as simple as attaching any tactile sensor to the feet of a robot. The sensors and the limbs need to have specific characteristics that support the implementation of the algorithms and allow the biped to safely come in contact with the terrain and detect the interaction forces. The challenges in handling the synergy of hardware and sensor design, and fabrication in a podotactile-based sensitive walking robot are addressed. The bipedal platform provides contact compliance through 12 series elastic actuators and contains 190 highly flexible tactile sensors capable of sensing forces at any incident angle. Sensitive walking algorithms are provided to handle multi-legged locomotion challenges including stairs and irregular terrain.

Acknowledgements

There are so many people who have made this project possible. To start I would like to thank my two advisors, Professor Eduardo Torres-Jara and Professor Stephen S. Nestinger. Both of you have been invaluable resources both in this project and my educational career. I'm really not sure where I would be right now if it wasn't for your guidance not only on this project but also on my career. You've made an impact probably more than you know. I thank you for that.

Next, thank you to my committee members, Dr. Gregory Fischer, Dr. John Sulivan and Dr. Simon Evans. The time you've spent going over my paper and giving me advice on how to improve it truly means a lot to me.

To my group partner Ennio – I couldn't have done it without you. I'm sorry for the hundreds of hours we've spent cabling and I'm sorry in advance for every time you'll have to redo a joint in the future. Thank you for being there to pull all-nighters with me whether it was because of the knee joint which just wouldn't tension properly, trying to figure out the proper inductance for the motor controllers or the hours we've spent figuring out the proper way to actually control this monster, I'm glad you were there to talk through things with me. I hope you have fun continuing this project and I'm sure we'll be working together in the future.

To Adriana – thank you for being patient with me. Thank you for bringing me food and making sure I was healthy when all I wanted to do was obsess over a problem. I'm happy you were there to look out for me.

Thank you to my family. Without your strive to push me into graduate school I would never be working on this great project and I would never be where I was today. Sorry for not calling as much as I should and falling off the face of the earth for a short while.

To all those that helped me with various forms of the design, modeling or assembling I am indebted. Allen, Nick, Brian and Mike thank you for the time you've spent helping me with simulations. Jon and Brian (again) thank you for the help you've put in looking through my design and reminding me that nothing ever works or looks good the first time you design it no matter how badly you want to be done. Thank you to Brennan, Nigel, and Paul for the help assembling the robot and figuring out the right tools for the job and to Catherine for the walking stance pictures. Nigel – you still owe me a 6-32 tap and a few threaded holes.

Thank you to Tracey – I've probably given you a full time job at this point just placing orders for me. I don't know how you manage to get anything done with my constant harassment of emails. You've been a pleasure to work with and I sincerely hope no other student harasses you as much as I have.

Finally, to Professor Gennert thank you for giving me the opportunities that you have. You've helped me quite a bit these last two years and I know for sure I would not have worked on this project if it wasn't for you. I hope the work I've produced can help grow WPI's programs.

Table of Contents

List of Figures

List of Tables

Chapter 1 Introduction

Legged locomotion is important in robotics because of the ability to adapt to varying terrain conditions. Legs work well indoors on flat floors and stairs, as well as outdoors on flat roads and rocky terrain. Moreover, about half of the Earth's landmass is currently inaccessible by wheeled or tracked vehicles [1], where legged animals move easily. However, some of the most advanced modern day legged robots are still incapable of ensuring stability while traversing irregular terrain. Legged robots, despite having the capability to overcome rough terrain are commonly not designed to interact with their environment. Many of these legged robots heavily rely on already knowing the terrain and walking with a predetermined gait. Even the slightest alteration in predicted terrain to actual terrain may cause the legged robot to fall down. Humans can deal with rough terrain with much greater ease, sensing environmental changes and adapting to unforeseen circumstances. Limited attention has been given to sensing the interaction between the foot and the terrain in legged robots; it is not common to equip a robotic foot with a large tactile sensor array.

Contact information becomes relevant on irregular terrain, which is exactly where legged locomotion is more effective than wheeled. For instance, human feet are covered by a large array of tactile sensors that provide information about the geometry of the floor (an edge, a flat surface), the force distribution throughout the foot (concentrated in the toe or heel), the stability of the contact (is it slippery?), and the presence of an obstacle in the trajectory (the toe touched a step). Contact information makes human walking adaptive [2]. Humans and other animals rely on touch for manipulation, grasping, and sensing the ground below them. This additional input has shown to be crucial for keeping balance in bipedal robots [3]. In fact, one of the leading solutions for bipedal navigation and balancing requires

the input of a limited number of on/off touch sensors to actively adjust the Zero Moment Point (ZMP) of the robot [4], [5], [6], [7] . These robots, while having good balance and control on fully level ground, still suffer from poor navigation capabilities on uneven terrain. On uneven ground, the limited on/off touch sensors do not provide useful information causing the robot to navigate blind and certainly fall.

The same problem was faced in robotic manipulation, where most of the traditional methods use little information about the contact interaction. Recent approaches use tactile feedback for some specific tasks in controlled experiments [8], [9], [10]. A more complete approach is sensitive manipulation [11], [12], [13], which uses tactile feedback in unstructured environments. Inspired by sensitive manipulation, this thesis addresses the development of an approach to robotic walking called *sensitive walking*. This approach uses podotactile feedback to effectively adapt robotic walking gaits to the possible variation in the terrain. In order to develop and test this approach, a bipedal robot has been designed and built with the required characteristics.

1.1 Literature Review

Legged locomotion has been and is still a major focus in robotics research. This section provides a comprehensive review on the history of legged robotic systems, tactile sensors, and control strategies for operating these difficult devices.

1.1.1 Legged Robots

Legged systems have been in development since the year 1850 when Pafnuty Chebyshev, a Russian mathematician, designed a linkage system to be used in a walking mechanism. Over the next 160 years, legged systems were further developed including the development of multiple biped and quadruped robots which successfully completed walking

and running gaits on a large array of complex terrain [14]. Legged systems have become more capable, completing more complex tasks with a high level of autonomy and intelligence. However, this was not a short journey, and required a number of significant jumps and contributions to the field. A summary of these contributions (current to 1997) is outlined in Table 1. While there are numerous other contributions over the past 15 years this list has not been recently updated and hence will only show contributions up to 1997. This section will further discuss other important milestones over the last 15 years.

Table 1: Summary of legged robotic milestones (adapted from [15])

Year	Inventor	Summary
1850	Chebyshev	Designs straight-line linkage used in early walking mechanism.
1872	Muybridge	Uses stop-motion photography to document running animals.
1893	Rygg	Patents human-powered mechanical horse.
1945	Wallace	Patents hopping tank with reaction wheels that provide stability.
1961	Space General	Eight-legged kinematic machine walks in outdoor terrain.
1963	Cannon and Higdon	Control system balances single, double, and limber inverted pendulums.
1968	Frank and McGhee	Simple digital logic controls walking of Phony Pony.
1968	Mosher	GE quadruped truck climbs railroad ties under control of human driver.
1969	Bucyrus-Erie Co	Big Muskie, a 15K ton walking dragline is used for strip mining.
1977	McGhee	Digital computer coordinates leg motions of hexapod robot walks with wave gait using digital computer to coordinate leg motion.
1977	Gurfinkle	Hybrid computer controls hexapod walker in USSR.
1977	McMahon and Greene	Human runners set new speed record on tuned track, compliance adjusted to mechanics of human leg.
1980	Hirose and Umetani	Quadruped machine climbs stairs and over obstacles using sensors.
1980	Kato	Hydraulic biped walks with quasi-dynamic gait.
1980	Matsuoka	Mechanism balances in the plane while hopping on one leg.
1981	Miura and Shimoyama	Walking biped balances actively in three-dimensional space.
1983	Sutherland	Hexapod carries human rider. Computer hydraulics and human share computing task.
1983	Odetics	Self-contained hexapod lifts and moves back end of pickup truck.
1983	Raibert	One-legged machine hops in place, travels at specified rate keeps its balance when disturbed, and jumps over small obstacles.
1984	Furusho	Planar five-link biped starts walking from a standing position, travels 0.8m/s.
1987	Waldron and McGhee	3ton self-contained hexapod carrying human travels 5mph in irregular terrain and pulls a load.
1988	Hodgins and Koechling	Planar biped climbs short stairway, jumps obstacles sets speed record of 13.1mph.
1989	Raibert	Quadruped runs with trotting, pacing and bounding gaits.
1990	McGeer	Planar biped with knees walks passively down sloping surface.
1991	Raibert	3D Biped travels around laboratory.
1992	Playter	3D Biped does 3D somersault.
1994	LegLab, 20th Cent. Fox	3D Biped and Uniroo appear in *Rising Sun* with Sean Connery.
1996	Leeser	Planar quadruped runs with articulated spine.
1997	Honda	Honda Motor Company announced its bipedal walking project which has resulted in an autonomous humanoid (ASIMO).

As Table 1 points out, the past two decades have shown a rapid movement to research and develop new more intelligent robotic systems with higher levels of autonomy. However, the design for a legged system is not without flaws. Major contributors to legged robots include Spring Flamingo [16], Asimo [3], and BigDog [17].

1.1.1.1 Spring Flamingo

Spring Flamingo shown in Figure 1, is a tethered planar bipedal robot developed at the MIT Leg Lab, as a robotic platform for the purpose of experimenting with walking algorithms, motion description and control techniques, and force control.

Figure 1: Spring Flamingo [16]

Spring Flamingo achieved a maximum walking speed of 1.2 meters/second while only using 15 watts of power as opposed to other bipedal robots which can draw over 200 watts [16]. Similar walkers have Spring Flamingo used a number of advanced strategies to more effectively control the robot's movement. Specifically, the implementation of series elastic actuators (SEAs) and the exploitation of passive dynamics proved to be a significant milestone in the field of legged robotics [18].

The traditional approach to controlling robotic arms and legs is to make the interface between the actuators and the load as stiff as possible. This method is one of the most commonly accepted for the development of a rigid, well composed robotic system [19], [20]. Low stiffness joints have their own respective advantages. An elastic element between the actuator and the load, commonly called a series elastic actuator, allows for greater shock resistance, lower inertia, better environment interaction and more stable force control techniques. Additionally, an elastic joint can tolerate mild irregularities in predicted contact points [16]. A block model depicting an SEA is given in Figure 2.

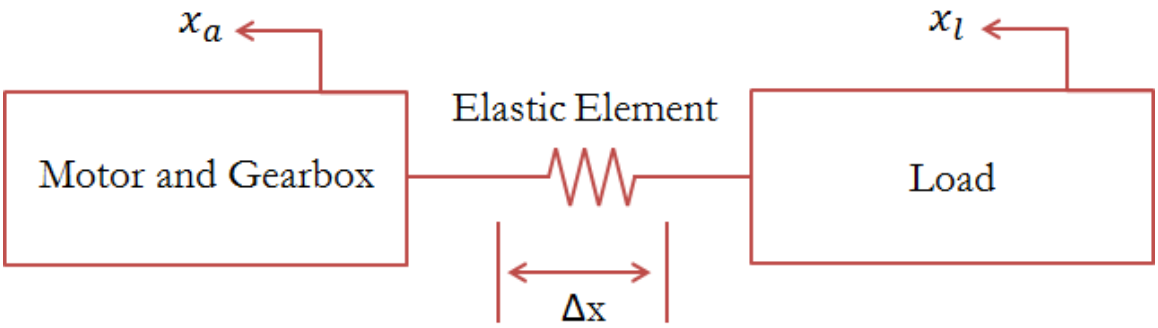

Figure 2: SEA block diagram [21]

Due to the elastic element, minor shock loads and torque ripples are strongly reduced. In essence, the elastic element acts as a mechanical low pass filter for vibrations. Additionally, with the aid of an SEA the force control problem is now turned into a position control problem, a much simpler problem to solve [21]. The force on the joint can be calculated knowing the spring stiffness, actuator position and load position using Equation (1)

$$F_J = k(x_A - x_L) \tag{1}$$

where F_J is the force on the joint, k is the spring stiffness, x_A is the position of the actuator and x_L is the position of the load. More directly, the force on the joint can be calculated by simply using Hooke's law and measuring the deflection on the spring.

The dynamics of many traditional robotic systems are commonly dominated by the inertia and friction characteristics of their actuators and not the actual dynamic characteristic of the system [16]. This can be a problem when trying to complete tasks such as letting a leg swing through its full natural motion without any powered control. In the case of traditional robotic systems, the negative effects of the dynamics of the actuators will commonly overpower any of the positive effects of the dynamics of the remainder of the developed system. SEAs negate the effects of some dynamic characteristics of the actuators by decoupling them from the load. Spring Flamingo uses series elastic actuators at each joint to help with exploiting the natural dynamics of its system. While Spring Flamingo was not the first to use compliance in a bipedal robot, the MIT Leg Lab effectively implemented SEAs and proved their effectiveness in a walking system [16], [18], [22], [23].

While Spring Flamingo was clearly a significant milestone in the development of bipedal robotic systems it is not without faults and serious limitations. Spring Flamingo is a fully tethered planar biped, walking around a boom with rotational joints in only one plane [16]. Additionally, Spring Flamingo cannot adjust to slopes of greater than 15 degrees and due to being a planar robot cannot interact to external forces in a non-planar dimension. This is due to the limited input the robot has with its environment. As shown in Figure 3, Spring Flamingo only uses two load cells to sense contact with the ground. While two load cells work to determine contact and pressure on perfectly flat ground, the model fails when interacting with rough terrain.

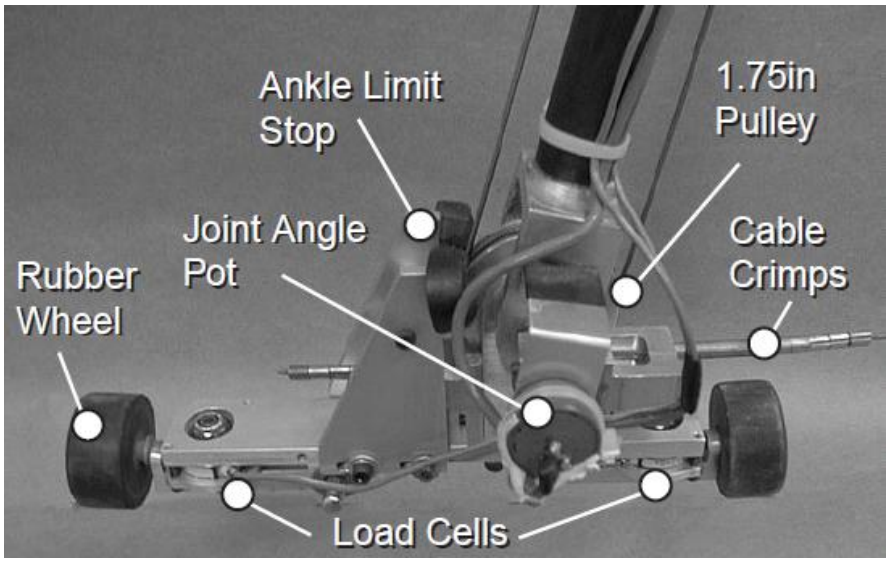

Figure 3: Detail of ankle on Spring Flamingo [16]

1.1.1.2 ASIMO

ASIMO, shown in Figure 4, is an advanced humanoid bipedal robot developed by Honda.

Figure 4: ASIMO Robot [3]

ASIMO, originally developed in 2000, is one of the most recognized humanoid robots effectively employing advanced dynamic balancing techniques. Since 2000, three significant revisions of ASIMO have been introduced in 2004, 2005 and 2011. The current version of ASIMO now weighs 48kg, runs 9 km/hour, operates for up to 40 minutes and contains 57 degrees of freedom. ASIMO contains six degrees of freedom in each leg, 3 located at the hip (spherical), one at the knee joint (front to back) and two at the ankle joint (front to back and left to right) [3]. For control, ASIMO uses a Zero Moment Point (ZMP) control strategy [24]. While the implementation of ZMP control has been previously demonstrated by a number of bipedal robots, ASIMO has proven to be one of the most effective and one of the few still in development [25], [26].

The center of mass can be defined as the average location of all individual mass particles in a system. More clearly this can be mathematically described as shown in Equation (2).

$$\overrightarrow{r_{com}} = \frac{\sum_i m_i \overrightarrow{r_i}}{M} \tag{2}$$

where i is each individual particle, m_i is the mass of each particle, $\overrightarrow{r_i}$ is the distance to each particle and M is the total mass of the system. Building upon the derivation of the center of mass the center of pressure can also be derived. The center of pressure is defined as the point on a system where the total sum of all the pressure fields will cause a force but no moment about that point. In the case of a legged robot walking over flat ground the center of pressure is equivalent to the ZMP of the system. The ZMP or center of pressure can then be mathematically defined as shown in Equation (3).

$$\overrightarrow{r_{cp}} = \overrightarrow{r_{ZMP}} = \frac{\sum_i F_{Ni} \overrightarrow{r_i}}{\sum_i F_{Ni}} \quad (3)$$

where F_{Ni} is the sum of the normal forces of each mass particle and all other terms are as defined in Equation (2) [4]. The zero moment point becomes crucial when trying to find a stable position for a bipedal robot. In order to be statically stable, defined as not tipping over, a robot's ZMP must be located fully within the support polygon of the robot. More so, it is desirable that the ZMP be located in the center of the support polygon. The support polygon is defined as the area of the extents of the foot placement of the robot as shown in Figure 5.

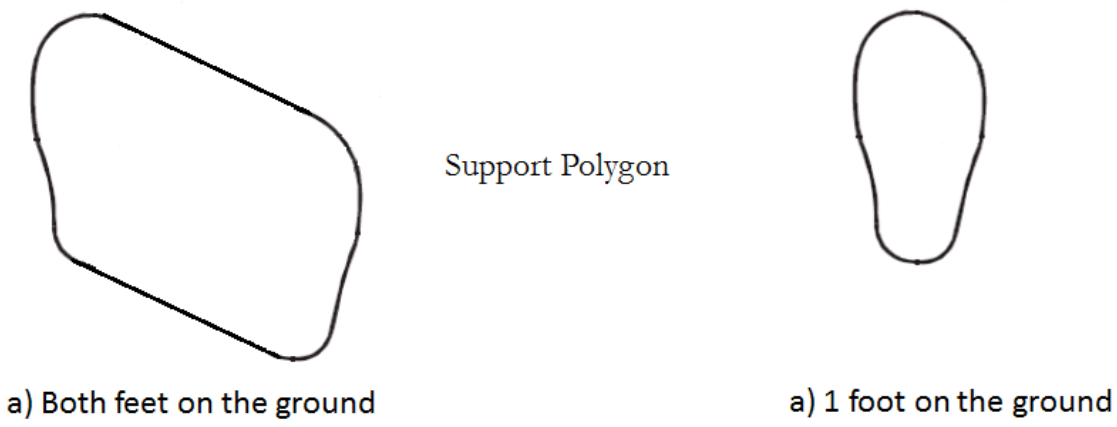

Figure 5: Support polygon of a biped taking a step.

When a bipedal robot takes a step, the support polygon is reduced down to the size of one foot. ASIMO, with the aid of a limited number of touch sensors in the corners on the bottom of the foot, effectively moves the ZMP of the system to constantly be located above the robot's support polygon. ASIMO balances using this ZMP control method rather than relying on force control or predetermined gaits using position control [24].

While ZMP control is clearly a step up from predetermined gaits, ASIMO still has failures. ASIMO walks in an inefficient manner and does not exploit the natural dynamics of

the system. ASIMO has failed on numerous accounts to walk up and down stairs and is not desgned on any environment harsher than stairs. These issues are due to the limited number of sensors prevalent on the soles of the feet. While ZMP control with this limited number of sensors works well on flat, even ground, the approach again fails when tackling uneven ground or staircases. In the case of stairs, ASIMO has a chance of not fully stepping onto the next step. Hence, the robot will surely fall due to the faulty readings from the sensors used to control the entire walking algorithm.

1.1.1.3 BigDog

BigDog, developed by Boston Dynamics (Waltham, MA), demonstrates the capabilities of a legged robot to overcome challenging uneven terrain. This quadrupedal robot, pictured in Figure 6, runs at 4 mph, climbs slopes of 35 degrees, and can successfully navigate through muddy and snow covered trails.

Figure 6: BigDog robot

BigDog is a hydraulically powered system where each compliant leg contains four active and one passive degree of freedom. BigDog implements a novel approach for dealing with challenging terrain by focusing on the foot placement to offset unwanted velocity changes in

the body. For example, as the robot begins to fall over in the lateral direction, the robot will stick out one of the feet to counteract the change in lateral body velocity. The emphasis on foot placement demonstrates a new approach to dynamic walking which has clearly shown to be effective at stabilizing a robot in dynamic situations [17].

1.1.1.4 Passive Dynamic Walkers

In 1990, Tad McGeer of the School of Engineering Science in British Columbia published an article arguing the existence of a certain subclass of two legged systems for which walking is a natural dynamic movement. When placed on a gentle slope a two legged system will walk under no additional power and no actuation using the natural dynamics of the system. McGeer proved these arguments by building a small bipedal robot with semi-circular feet [27]. In the same year, McGeer furthered this claim by stating that a passive dynamic walker can also be built with a locking knee [28].

One way to look at a passive dynamic walker is to envision it as a rimless wheel as shown in Figure 7. In this model we are presented with a wheel with spokes of negligible weight, length l, offset between links of 2α and slope angle to the ground of γ. Additionally, the top spoke of the rim forms an angle θ relative to the normal of the ground plane.

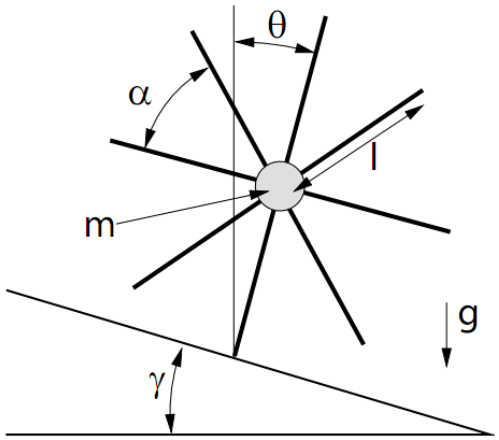

Figure 7: Rimless wheel model [29]

In this case, the rimless wheel exhibits velocity which is dictated by the spoke length l, and slope angle γ. The dynamics of the system have proven to be stable [27]. The rimless wheel model can be further expanded to represent a bipedal system walking down a slope. If the rimless wheel model is modified to use only two of the spokes with a pin joint in between them, the entire system can be represented as a dynamically stable compass gait as shown in Figure 8. In this case, the mass of the system is represented as a mass along each leg denoted m and a mass at the center of the body denoted m_h. Each leg also forms its own angle relative to the slope denoted θ_{sw} and θ_{st} for the back and front leg respectively [27], [29]. This model can be further expanded to include a locking knee joint [28]. Through simulations and realized models, researchers have proven that by exploiting the natural dynamics of the system a dynamically robot can walk in a stable manner even over moderately uneven ground [27], [28], [30], [31]. Researchers have proved that sloped ground is not necessary and low power mechanical actuators can be used to make the robot walk over flat ground [32], [33]. Understanding that passive dynamics can be used to more easily and efficiently control a bipedal robot will be valuable information to take into account in the design and controls of the proposed bipedal system.

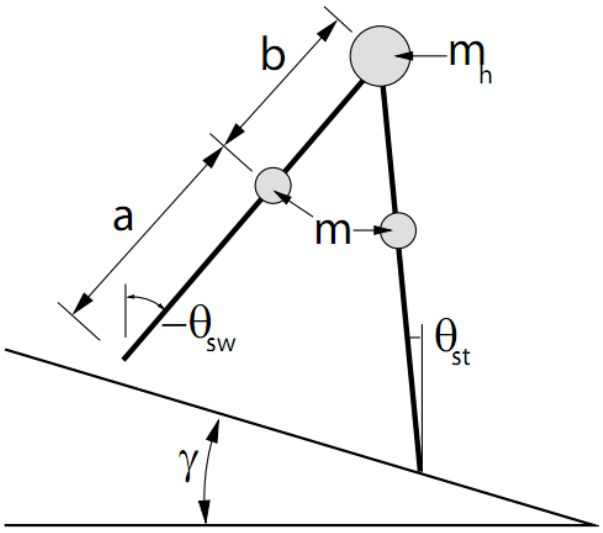

Figure 8: Compass gait model [29]

1.1.2 Tactile Sensors

Numerous researchers have shown the importance of tactile sensing in manipulation. Precision control with the use of force sensing can be helpful to accurately manipulate objects. The importance of force sensing can be easily shown in human manipulation. When human fingers are anesthetized they become clumsy due to their unreliable feedback [34]. In order to be effective, the tactile sensors must be flexible and easily deflect when coming in contact with any obstacle. The following sections serve as an overview of the various tactile sensors that have been implemented and their respective qualities.

1.1.2.1 Tactile Sensing in Humans

Much inspiration has come from humans when developing touch sensors for robots. Humans are able to sense and interact with their environment because of their increased awareness gained through touch. Mechanoreceptors within human skin, as shown in Figure 9, sense contact and are able to detect a variety of object properties including shape, size,

texture, temperature, and position. These receptors can be used as motivation for designing tactile sensors in robotic systems.

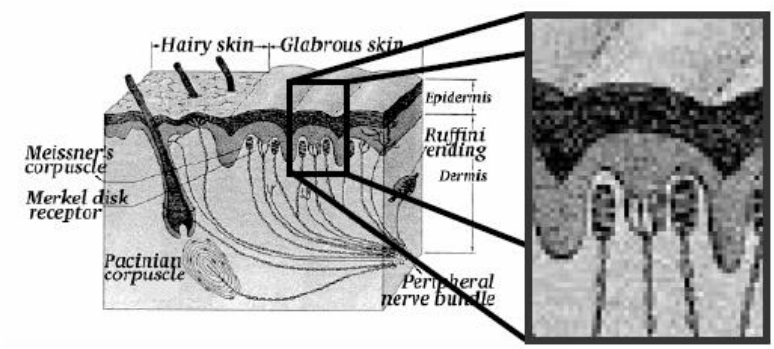

Figure 9: Illustration of a mechanoreceptor [12]

1.1.2.2 Tactile Sensing in Robotic Systems

The use of tactile feedback in robotic manipulators has been extensively explored [35]. A number of different technologies have been explored and fully exploited as possible solutions of gaining feedback from the environment. Technologies for sensing contact include piezoelectric sensors [36], optical sensors [37], strain gages, force sensing resistors (FSRs) [38] and numerous others. A more complete review of tactile sensing technology in robotic systems can be found in [35]. Developed by Eduardo Torres-Jara, is a more complete approach to robotic manipulation which uses tactile feedback in unstructured environment. Sensitive manipulation has been proven effective in a number of robotic platforms including the humanoid robot Obrero [13] and the GO playing robot GOBot [11] pictured in Figure 10 and Figure 11, respectively.

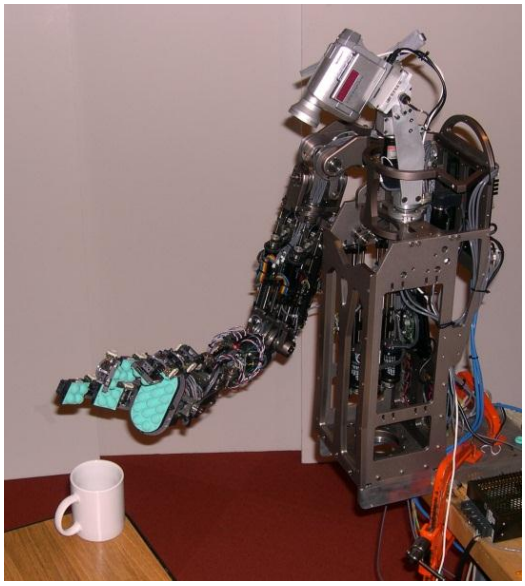

Figure 10: Obrero Robot [13]

Figure 11: Go-bot Robot [11]

Obrero uses a magnet and four hall-effect sensors to localize the position of a force vector on the gripper. The sensors and magnet are encapsulated in a flexible hemispherical dome. GoBot, improves on this technology by using four phototransistors and one infrared led which measures the diffraction off the hemispherical dome. An illustration of the sensors used in GoBot is shown in Figure 12. These sensors are low cost and very simple to manufacture. Extending on the principle of tactile sensing in robotic manipulation, limited attention has been given in tactile sensing in legged robotics.

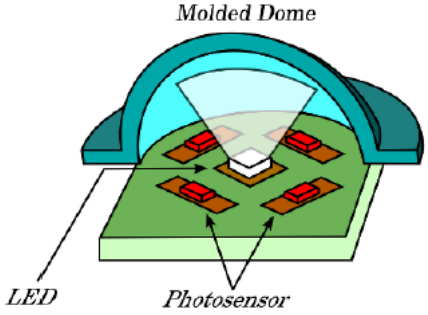

Figure 12: Low cost omnidirectional tactile sensor

In general, legged robotic systems have given limited attention to the interaction between the foot and the terrain. Foot interaction has been represented as a single point of contact [39], three points of contact [40], or four points of contact in a rectangular array [3]. A limited amount of research has been conducted in having a large force sensing resistor array on the foot of a walking system. This research focused on developing pressure maps indicating the foot pressure distribution under static loading [8].

1.2 Thesis Contributions

In the past, limited attention has been given to sensing the feet-terrain interaction in robotics. This thesis introduces a paradigm shift in robotic walking called *sensitive walking* realized through the development of a compliant bipedal platform. This approach utilizes podotactile feedback to enhance real-time walking stability by effectively adapting to variations in the terrain. Adapting legged robotic platforms to sensitive walking is not as simple as attaching any tactile sensor to the feet of a robot. The sensors and the limbs need to have specific characteristics that support the implementation of sensitive walking algorithms.

This thesis focusses on the mechanical design and analysis of a robotic platform for sensitive walking. The thesis presents a kinematic and dynamic model of a new state-of-the-art bipedal sensitive walking platform. The model is presented, explored and analyzed in full detail. The mechanical design for this robot has been presented and explained. Actuator component selection and their justifications are presented. This thesis also discusses the assembly of the full robot. Analysis on the design, initial failures and future improvements are also given. Finally, sensitive walking algorithms are provided to handle bipedal locomotion challenges including stairs and irregular terrain. This thesis does no go in depth

on the electronic or software architecture of the system. While the thesis explains the basics of the design it was not within the scope of the project to focus on sensor integration or system architecture.

1.3 Thesis Layout

The remainder of the thesis is organized as follows. Chapter 2 introduces a kinematic and dynamic model of the bipedal robot, and a foot pressure distribution model. Chapter 3 provides the justification behind the mechanical and electrical design of the robot and a full system overview. Chapter 4 introduces the sensitive walking approach and provides a few specific example algorithms. Chapter 5 covers the experimental validations and results of the realized system. Chapter 6 concludes the thesis and offers suggestions for future work on the project.

Chapter 2 Kinematic and Dynamic Modeling

This chapter addresses the kinematic and dynamic model for the legged robot pictured in Figure 13. The section begins by introducing Denavit-Hartenberg parameters followed by both the forward and inverse kinematics of the system. The dynamics of the system are then derived and implemented in a MATLAB simulation. Finally a static pressure distribution of the foot is derived

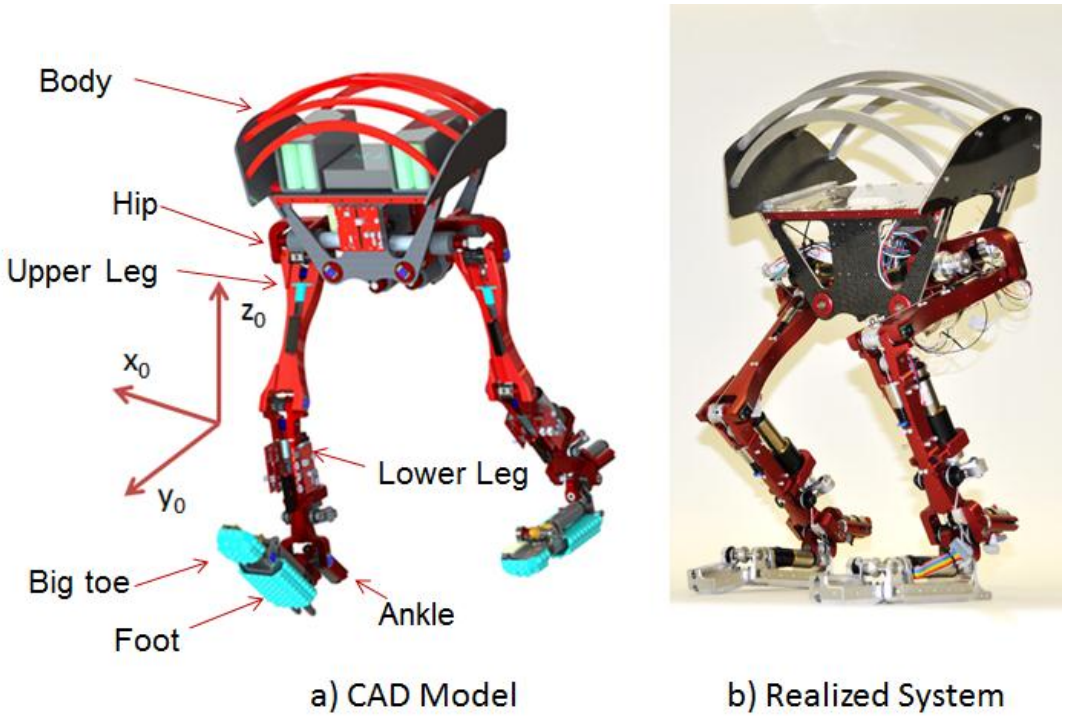

Figure 13: Bipedal robot designed for sensitive walking.

2.1 Denavit-Hartenberg Parameters

A robotic manipulator is comprised of a set of links coupled by various styles of joints. This bipedal robot will be composed of seven links on each leg coupled by six revolute joints. The rationale for all design decisions including joint positions and angles will be

further addressed in Chapter 3. Denavit-Hartenberg parameters (DH parameters) were used for the purpose of being able to represent transformations in the leg as a result of joint angles.

The DH parameters are a particular convention associated with attaching together kinematic chains. In this case there are four parameters which can fully define the transformation between two joints. The parameters θ, α, a, and d are the DH parameters of the system where θ represents the joint angle, α represents the link twist, a represents the link length, and d represents the link offset [3]. Using the standard DH convention a set of coordinate axes was determined for each leg. Figure 14 illustrates the layout for the coordinate frames for this particular robot. Note that only the z axis has been drawn into the picture for the purpose of reducing clutter.

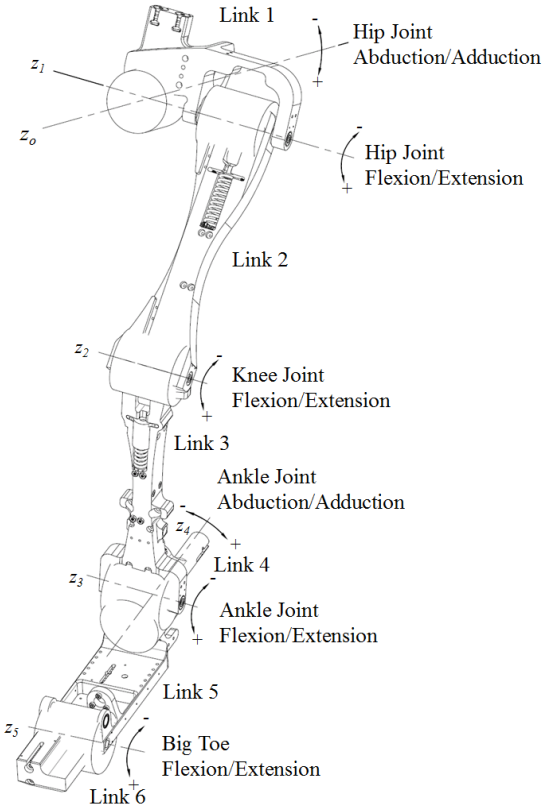

Figure 14: Leg coordinate axes

Using Figure 14 the associated DH parameters for the robot are provided in Table 2.

Table 2: Denavit-Hartenberg parameters of one leg of the biped robot.

θ (radians)	*a (meters*	*d (meters*	α (radians)
$\boldsymbol{\theta_1(t)}$	0	0	$\frac{\pi}{2}$
$\boldsymbol{\theta_2(t)}$	0.21	0.08	0
$\boldsymbol{\theta_3(t)}$	0.22	0	$\frac{\pi}{2}$
$\boldsymbol{\theta_4(t)}$	0.02	0	$\frac{-\pi}{2}$
$\boldsymbol{\theta_5(t)}$	0.03	0.14	0
$\boldsymbol{\theta_6(t)}$	0.02	0	0

2.2 Forward Kinematics

Next the forward kinematics of the system were determined. Each joint is represented as a number from 1 to *n* and each link from 0 to *i* with 0 representing the first link and *i* representing the final end effector (the foot). Link 0 will be considered the ground of the system and all transformations will be initially based off of its position. Furthermore, each link *i* is based off of the reference frame defined by the previous link *i-1*. Each joint transformation can be denoted as a transformation q_i . In the case of a revolute joint, q_i is the revolute transformation denoted as θ_i. Alternatively, prismatic joints are denoted by d_i. It is possible to represent the kinematic chain as a serial chain of *n* links with the transformation matrix T_j^i given in Equation (4).

$$T_j^i = \prod_{i=1}^{n} T_i^{i-1}(q_i) \tag{4}$$

Each transformation represents a translation about the z-axis, Equation (5), a translation about the x-axis, Equation (6), a rotation about the z-axis, Equation (7) or a rotation about the x-axis, Equation (8).

$$Translation_z = \begin{bmatrix} 1 & 0 & 0 & 0 \\ 0 & 1 & 0 & 0 \\ 0 & 0 & 1 & d_i \\ 0 & 0 & 0 & 1 \end{bmatrix} \tag{5}$$

$$Translation_x = \begin{bmatrix} 1 & 0 & 0 & a_i \\ 0 & 1 & 0 & 0 \\ 0 & 0 & 1 & 0 \\ 0 & 0 & 0 & 1 \end{bmatrix} \tag{6}$$

$$Rotation_x = \begin{bmatrix} 1 & 0 & 0 & 0 \\ 0 & \cos\alpha_i & -\sin\alpha_i & 0 \\ 0 & \sin\alpha_i & \cos\alpha_i & 0 \\ 0 & 0 & 0 & 1 \end{bmatrix} \tag{7}$$

$$Rotation_z = \begin{bmatrix} \cos\theta_i & -\sin\theta_i & 0 & 0 \\ \sin\theta_i & \cos\theta_i & 0 & 0 \\ 0 & 0 & 1 & 0 \\ 0 & 0 & 0 & 1 \end{bmatrix} \tag{8}$$

The full homogenous transformation can be represented as a product of the four transformations denoted A_i shown in Equation (9).

$$T_i = \begin{bmatrix} \cos\theta_i & -\sin\theta_i\cos\alpha_i & \sin\theta_i\sin\alpha_i & a_i\cos\theta_i \\ \sin\theta_i & \cos\theta_i & -\cos\theta_i\sin\alpha_i & a_i\sin\theta_i \\ 0 & \sin\alpha_i & \cos\alpha_i & d_i \\ 0 & 0 & 0 & 1 \end{bmatrix} \tag{9}$$

The homogeneious transformation T_i can be broken up as shown in Equation (10) where $R \in \mathbb{R}^{3x3}$ rotation matrix and $D \in \mathbb{R}^{3x1}$ translation matrix.

$$T_i = \left[\begin{array}{c|c} R & D \\ \hline 0 & 1 \end{array}\right] \tag{10}$$

.

Equation (4) was then applied to find the position of each individual joint from a ground reference plane. An additional transformation was added to have the origin of the system be located at the center of gravity of the robot, with the robot walking along the y-axis and standing in the z-axis. A representation of the system with appropriate link lengths and coordinate axes was then visualized in MATLAB. A figure of the forward kinematics model with the coordinate frame of each link can be seen in Figure 15. Only the top 3 joints are shown since the remaining joints affect only the orientation of the leg.

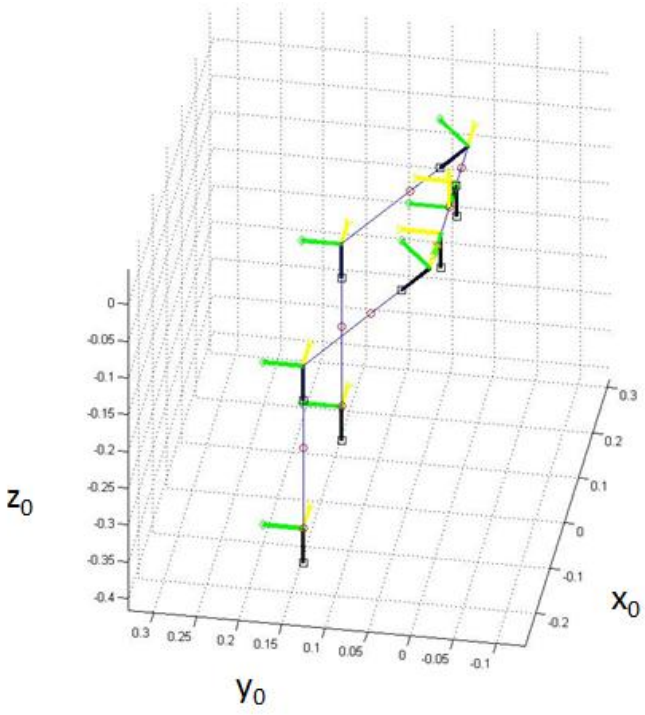

Figure 15: Visualization of the biped robot.
For each link: Black arrows are the x-axis, green arrows are the y-axis, yellow arrows are the z-axis. Red markers represent the CG of each link.

Figure 15 represents the solution to the forward kinematics problem. Hence, given the angle of each joint the end position of each link can be calculated. A full MATLAB script for the homogeneous transformations of all six links is provided in Appendix A: Forward Kinematics.

2.3 Inverse Kinematics

Inverse kinematics is the solution to the problem of finding the joint angles of the system given the final end effector position. The solution is important to allow the robot to decide where to move the joints given a certain trajectory for the foot to follow. Many manipulators are kinematically redundant and have more than one solution for the final end effector position. A demonstration of kinematic redundancy in a robotic manipulator can be seen in Figure 16.

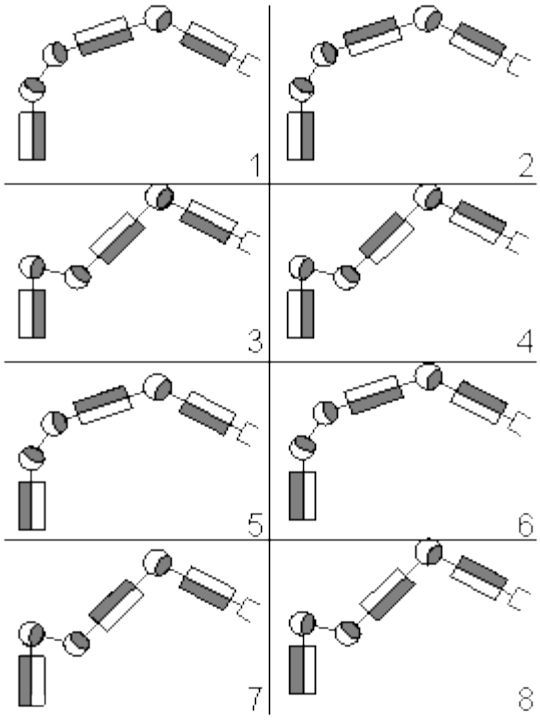

Figure 16: A kinematically redundant arm [41].

From Figure 16, multiple configurations will lead to the exact same final position. In many cases it is advantageous to choose one configuration over another. While the developed biped robot contains six degrees of freedom per leg, many are irrelevant for gait generation. For example, the hip abduction/adduction and the ankle abduction/adduction are used to stabilize the robot through orientation. The big toe is irrelevant for gait

generation and the ankle flexion/extension is used to orient the position of the foot. Knowing these facts, the system is reduced to a two degree of freedom planar linkage. While there are still two solutions, one can be eliminated due to the physical limitations of the system. Hence, the system is left with one closed-form solution for the two joint angles denoted as θ_2 and θ_3 which can be solved using a geometric approach. Figure 17 illustrates the system parameters. In this case, the final given variables are the components of the end effector's positions (x,y), the link lengths l_1 and l_2. The goal is to find the two unknown angles θ_2 and θ_3.

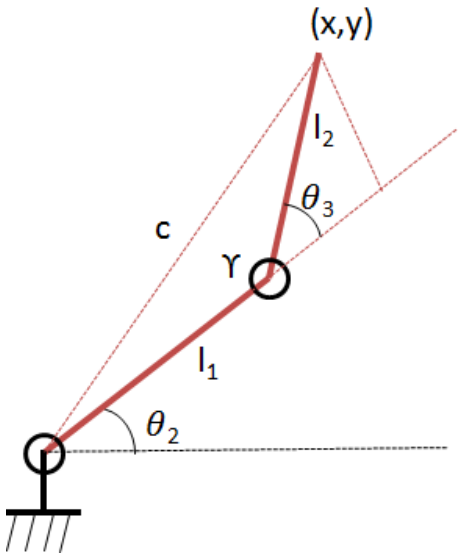

Figure 17: Two degree of freedom planar linkage.

By drawing line c which is equivalent to x^2+y^2 the law of cosines can now be used to compute angle γ as demonstrated in Equation (11). Terms are then rearranged and θ_3 is directly solved for in Equation (12).

$$x^2 + y^2 = l_1^2 + l_2^2 - 2l_1 l_2 \cos(\gamma) \tag{11}$$

$$\theta_3 = \cos^{-1} \frac{x^2 + y^2 - l_2^2 - l_1^2}{2l_1 l_2} \tag{12}$$

While there is a second solution to this problem called the "elbow up" configuration, the mechanical limitations of the robot do not allow the leg to reach this alternative position. Having solved for θ_3, θ_2 can now be solved for using the law of sines. The solution is given in Equation (13).

$$\theta_2 = atan(y/x) - atan(l_2 sin\theta_3/(l1 + l2\cos\theta_3)) \tag{13}$$

These equations have been implemented and verified in a MATLAB simulation of the robot walking through an elliptical gait pictured in Figure 18. The figure shows two frames of the leg of the robot following a trajectory of an ellipse where the x and y positions are parametrically defined. The full code for the system is provided in Appendix B: Inverse Kinematics.

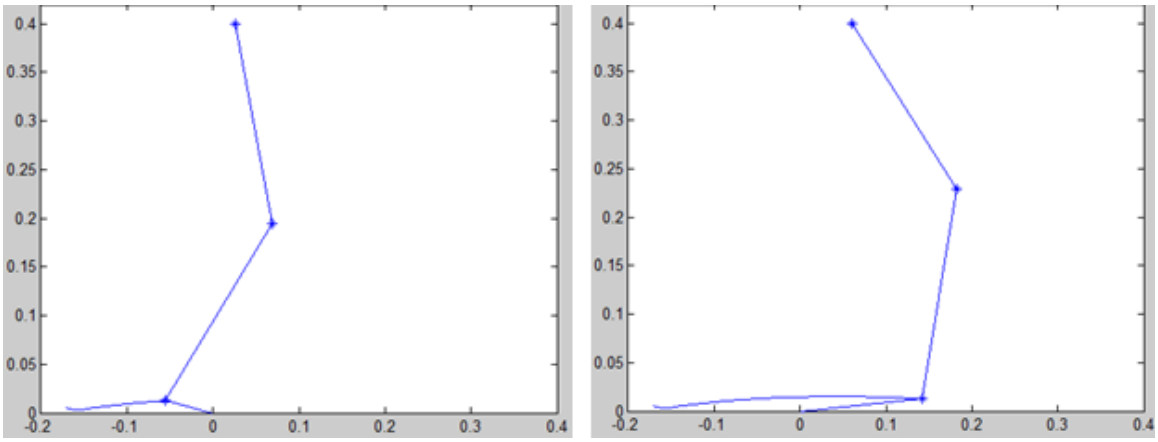

Figure 18: MATLAB simulation of inverse kinematics implemented into an elliptical gait

2.4 Dynamic Model

The dynamics of the system can be calculated using the equations of motion of the system as shown in Equation (14).

$$M(q)\ddot{q} + C(q,\dot{q}) + g(q) = S^T\tau \tag{14}$$

where

- $M \epsilon \mathbb{R}^{nxn}$ is the mass matrix

- $C \in \mathbb{R}^{nx1}$is the coriolis and centrifugal components
- $G \in \mathbb{R}^{nx1}$ is the gravitational components
- $S^T \in \mathbb{R}^{kxn}$ is the selection matrix of the actuated joints
- $\tau \in \mathbb{R}^{kx1}$ are the generalized forces
- n are the number of independent joint variables

In this case the goal is to solve for the generalized forces of the system such that a controller can be developed, appropriate actuators can be sized, and a mechanical design can be developed to appropriately fit the forces expected on the system. A number of approaches can be taken to solve the dynamic model of the system including Euler-Lagrangian dynamics, Newton-Euler dynamics, or Kane's method [42]. In this case Kane's method is a more suitable solution to the problem. Lagrangian dynamics relies on calculating the kinetic and potential energies of each link in the system throughout the gait. Due to the floating body, actively recalculating potential and kinetic energies in the system becomes very difficult and computationally intensive. Newton-Euler dynamics are also not ideal due to similar complexities. As such, Kane's method was used which relies on building up a kinematic model of the system. These formulations will allow for the solution to the mass matrix, coriolis and centrifugal components and gravitational components. Kane's method is a projection of the conservation of impulse and angular moment onto the generalized coordinate frame. The formula follows the form shown in Equation (15).

$$\sum_{i=1}^{N} J_{S_i}^T p_i + J_{R_i}^T N_{S_i} - J_{S_i}^T F_{S_i}^a - J_{R_i}^T T_i^a = 0 \tag{15}$$

The impulse is further expanded in Equation (16) and the angular momentum further expanded in Equation (17),

$$p_i(q) = m_i \dot{r} os_i \tag{16}$$

$$N_{S_i} = \theta_{S_i} \Omega_i \tag{17}$$

where r is the position vector of the system, $\dot{r}$ is the derivative of the position vector represented as the velocity, Ω is the angular velocity of each link, p is the impulse of each individual link, m is the mass of each link, S_i represents the center of gravity of each link I and J^T represents the Jacobian transpose of the system. The Jacobian of the system is calculated by Equation (18).

$$J(q) = \frac{\partial r\,(q)}{\partial q} = \begin{pmatrix} \frac{\partial r_1}{\partial q_1} & \frac{\partial r_1}{\partial q_2} & \cdots & \frac{\partial r_1}{\partial q_n} \\ \frac{\partial r_2}{\partial q_1} & \frac{\partial r_2}{\partial q_2} & \cdots & \frac{\partial r_2}{\partial q_n} \\ \vdots & \vdots & \ddots & \vdots \\ \frac{\partial r_m}{\partial q_1} & \frac{\partial r_m}{\partial q_2} & \cdots & \frac{\partial r_m}{\partial q_n} \end{pmatrix} \tag{18}$$

The Jacobian is used to map the generalized velocities to the Cartesian velocities, Equation (19), and map the Cartesian forces to the generalized forces, Equation (20).

$$\dot{r} = J\dot{q} \tag{19}$$

$$\tau = J^T F \tag{20}$$

It is also known that impulse and angular momentums of the system can be described in Equations (21) and (22)

$$\dot{p}_i = m_i \ddot{r} os_i \tag{21}$$

$$\dot{N}_{S_i} = \theta_{S_i} \dot{\Omega}_i + \Omega_i \times \theta_{S_i} \Omega_i \tag{22}$$

where θ_{S_i} is the inertia of body *i* with respect to the center of gravity. Finally, using the kinematically derived relations as shown in Equations (23), (24), and (25)

$$\ddot{r} os_i = J_{S_i} \ddot{q} + \dot{J}_{S_I} \dot{q} \tag{23}$$

$$\Omega_i = J_{R_i}\dot{q} \tag{24}$$

$$\dot{\Omega}_i = J_{R_i}\ddot{q} + \dot{J}_{R_i}\dot{q} \tag{25}$$

the mass matrix, coriolis and centrifugal terms and gravitational components are solved for as shown in Equations (26), (27), and (28) respectively.

$$M(q) = \sum_{i=1}^{N} J_{S_i}^T m_i J_{S_i} + J_{R_i}^T \theta_{S_i} J_{R_i} \tag{26}$$

$$\mathrm{C(q)} = \sum_{i=1}^{N} J_{S_i}^T m_i \dot{J}_{S_I}\dot{q} + J_{R_i}^T \theta_S \dot{J}_{R_i}\dot{q} + \Omega_i \times \theta_{S_i}\Omega_i \tag{27}$$

$$g(q) = \sum_{i=1}^{N} -J_{S_i}^T F_{S_i}^g \tag{28}$$

Now, knowing the formulas for the mass matrix, *M*, coriolis and centrifugal matrices, C, and gravitational matrices, *g*, it is possible to solve for the generalized forces τ. The inertial quantities presented in Table 3 were calculated with the aid of SolidWorks and are used as the inputs to the system. A simplified CAD model was developed for each link of the system. In order to achieve accurate center of gravity and moment of inertia values, a coordinate axis needed to be set up to follow the notation previously determined by the Denavit-Hartenberg notation.

Table 3: Robot parameters necessary for dynamic calculation.

Body Part	Length (m)	Mass (kg)	CGx (m)	CGy (m)	CGz (m)	Ixx ($kg*m^2$)	Iyy ($kg*m^2$)	Izz ($kg*m^2$)
Body	0.057	4.916	-0.001	0.117	0.011	0.112	0.044	0.130
Hip	0.078	0.995	0.031	0.029	0.007	0.003	0.002	0.003
Upper Leg	0.210	0.468	0.097	0.000	-0.003	0.000	0.007	0.006
Lower Leg	0.221	0.729	0.113	0.018	0.005	0.001	0.011	0.011
Ankle Joint 1	0.018	0.236	-0.042	0.040	-0.013	0.001	0.001	0.001
Ankle Joint 2	0.030	0.401	0.027	0.004	0.060	0.002	0.002	0.000

A MATLAB model was developed to calculate the dynamics of the bipedal system while walking through a selection of gaits. The full implementation of the dynamic model of the system is provided in Appendix C: Dynamic Simulation Code.

2.5 Pressure Distribution over the Foot

Using the dynamic model, a static foot pressure distribution model was also developed. The model predicts the expected pressure on each portion of the foot as the body moves relative to the foot. The analysis was conducted using a simple moment balance. First a free body diagram of the entire system was drawn as shown in Figure 19.

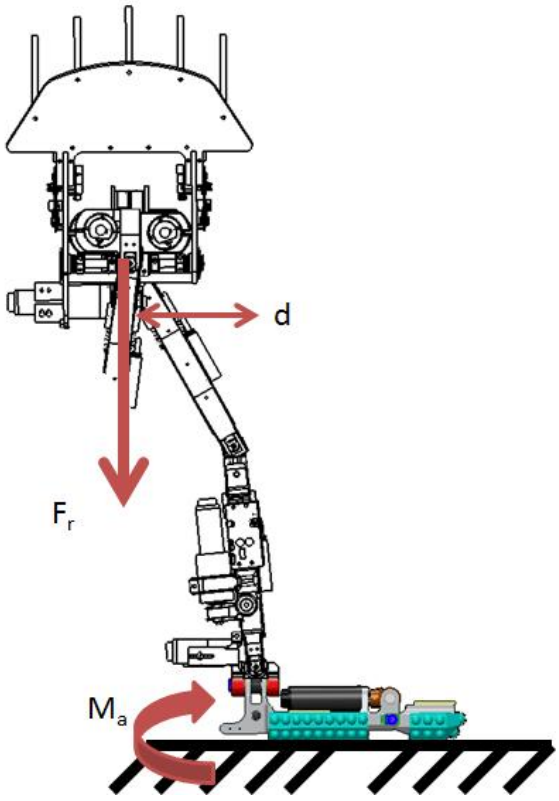

Figure 19: Moment balance of robot with one foot

The force, F_r, represents the total force of the robot at the center of gravity point, M_a represents the moment exerted at the ankle to keep the system balanced and d represents

the distance between the ankle joint and the center of gravity. Using Figure 19, it is clear that M_a can now be represented as being equivalent to F_r*d. Understanding that the full weight of the robot will be taken up by the one foot and knowing that there will be a linear force distribution, represented as ax+b, along the foot the total force of the robot can be represented as in Equation (29). The distribution will be linear since there is only one force acting at a distance implying a linear distribution.

$$F_r = \int_{x_1}^{x_2} (ax + b)dx \tag{29}$$

where x_1 is the beginning of the foot contact point and x_2 is the tip of the foot. Likewise, it is possible to solve for the moment balance in the system using (30).

$$M_a = \int_{x_1}^{x_2} x(ax + b)dx \tag{30}$$

To find the pressure distribution, it is necessary to solve for a and b. Since the system now reduces to two unknowns, a and b, with two equations, (29) and (30), a simple algebraic manipulation was necessary to solve for a and b. The two solutions are given by Equations (31) and (32).

$$a = \frac{6F_r(x_1 - 2d + x_2)}{(x_1 - x_2)^3} \tag{31}$$

$$b = \frac{2F_r(2x_1^2 + 2x_1x_2 - 3dx_1 + 2x_2^2 - 3dx_2)}{(x_1 - x_2)^3} \tag{32}$$

This pressure distribution on the foot was validated using a MATLAB simulation which would move the body of the robot relative to a stationary foot. The distribution on the foot could be observed to change as a function of the robot moving its position. The data was further validated by observing that, as expected, the pressure distribution, at the center of the foot was even across the entire foot. Figure 20 illustrates multiple frames in the

MATLAB simulation. The simulation depicts the planar pressure on the bottom of the foot as the robot's body moves from left to right over the foot.

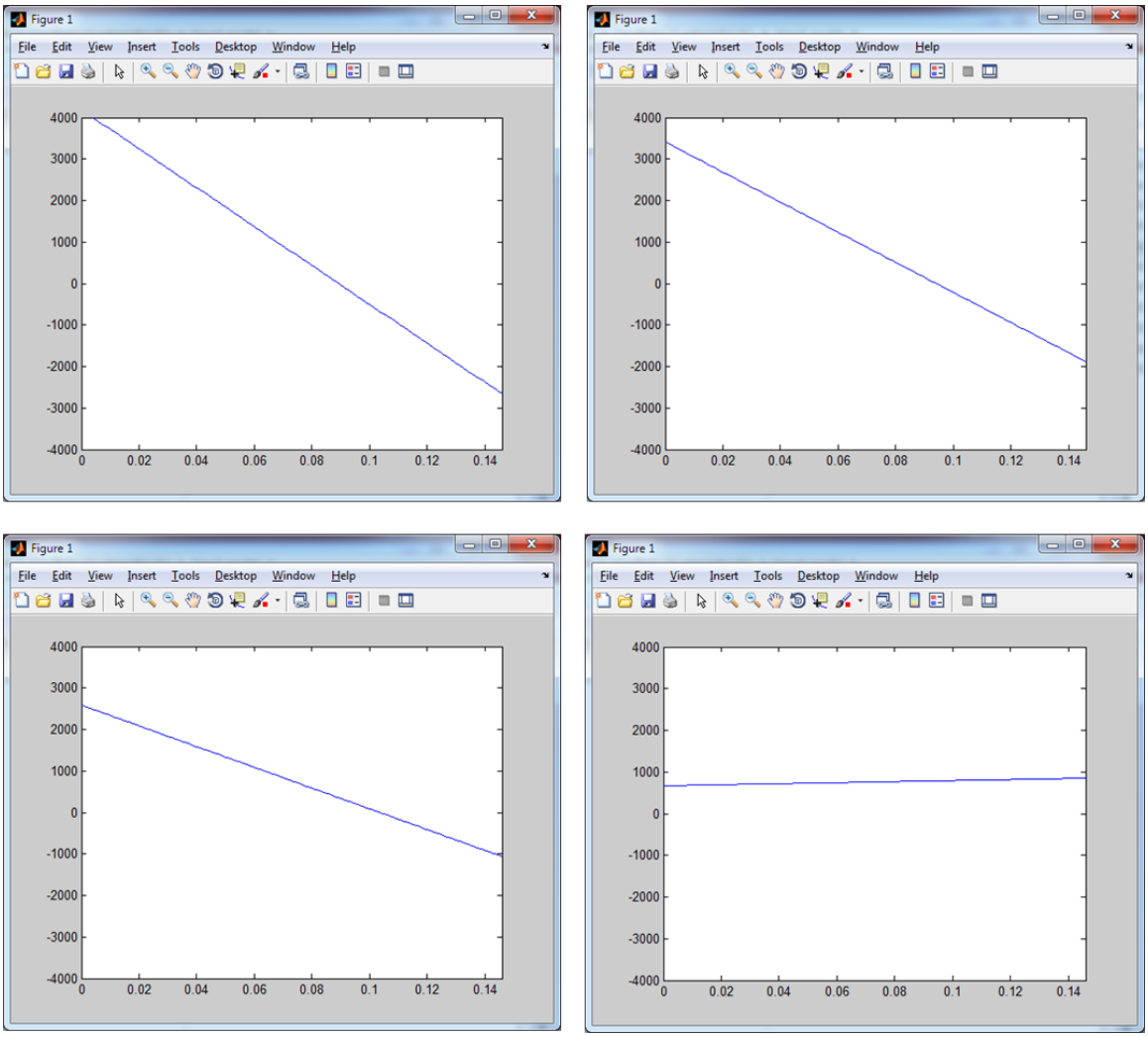

Figure 20: Stop motion animation of force distribution in foot.
Line depicts pressure on each section of the foot

Chapter 3 Mechanical Design & Electrical Architecture

This chapter addresses the mechanical and electrical architecture for a bipedal sensitive walking platform. The section begins by discussing the design parameters for the system. The next section discusses the details of the mechanical design of the system including spring selection, actuator selection and component design and analysis. Finally, the electrical system architecture is discussed and justification is given for the decisions pertaining to the architecture.

3.1 Design Parameters and Justifications

The sensitive walking platform was designed to walk with the help of tactile feedback in unstructured environments. The sensitive walking approach uses podotactile feedback to effectively adapt robotic walking gaits to the possible variation in the terrain. Adapting legged robotic platforms to sensitive walking is not as simple as attaching any tactile sensor to the feet of a robot. The sensors and the limbs need to have specific characteristics that support the implementation of the algorithms. As such a set of strict design criterion have been set to ensure success in sensitive walking. They are as follows:

This robot must be designed as a passive dynamic walker. This is to allow for a simpler control system which incorporates the natural dynamics of the system and a passive swing leg phase. Passive dynamic walkers, if designed correctly, will use significantly less energy than their active walker counterparts.

To mimic the major degrees of freedom in a human leg the robot must contain five degrees of freedom per leg. Specifically, there must be two degrees of freedom at the hip, one degree of freedom at the knee and two degrees of freedom at the ankle. An additional degree of freedom must also be implemented into an actuated big toe. The big toe provides critical information with regards to the walking stride, the ability to explore the environment through tapping, and minute gait control for stability purposes.

The robot must roughly mimic a toddler both in size and weight. A limit of 13 kilograms in mass and 1 meter in height have been set as guidelines for the robot parameters. The weight and size are set to keep cost low and allow one person to feasibly work on the robot.

The robot must contain Series Elastic Actuators (SEAs) at each joint to allow for a compliant robot capable of coming in contact and interacting with its environment. The justification behind employing SEAs is presented in Section 3.2.1 Series Elastic Actuators.

The robot must be untethered. Many modern day robotic systems rely on external power and tethering in a highly structured environment to locomote. In order to ensure that this robot will see the outside world and conquer difficult terrain, it must be capable of leaving the laboratory setting and moving into the real world. As such, all processing will be computed on-board and power to the system will be delivered with a set of on-board batteries.

The feet of the robot must be lined with highly compliant tactile sensors allowing the robot to interact and adapt to a dynamic environment. In order to sense the environment, the robot must detect everything within its surroundings. Specifically, the sensors must be able to detect contact at any incident angle and slipping.

The success of the sensitive walking platform will be gauged on the completion of these design parameters. The mechanical design, electrical design and software architecture must reflect these design parameters and be deeply integrated to ensure their success.

3.2 Mechanical Design

3.2.1 Series Elastic Actuators

Given the design requirements for the system, series elastic actuators were designed for each link of the system. The simplest SEA uses two torsion springs in-line with the motor and connected to the load. However, this solution is usually bulky and not very robust if using Commercial-Off-The-Shelf (COTS) parts, or very expensive if designing custom springs. Instead, traditional die compression springs on a rotary pivot can be used to substitute the torsion springs. Extension springs are also poor choices for these applications due to their poor energy density and poor construction. Compression springs are especially advantageous due to their low cost, inherent robustness and high energy density. There still lies a significant challenge on how to cleanly integrate springs into the design of the system. Many attempts have been made to cleanly integrate SEAs into the design of a robotic manipulator. However, most SEA's end up being very large [16], [42].

The sensitive walking platform used a new SEA design inspired by the legged robot Spring Flamingo [16], and the humanoid robot Obrero [12]. A cable system is used to pull on two compression springs cleanly embedded into each joint. An example of how the SEA is implemented into all six joints is discussed in the following subsections.

With the use of SEAs, it is very important to be able to sense the force on the system. Every joint on the system senses force with the use of a linear potentiometer mounted directly on the spring. It is especially important to mount a potentiometer on the

spring rather than calculate the displacement between the actuator and the load. Mechanical imperfections cause the latter method to yield unreliable data leading to an uncontrollable system. The following sections address integration of SEAs into each joint: hip abduction/adduction, hip flexion/extension, knee flexion/extension, ankle flexion/extesnsion, ankle abduction/adduction and the big toe.

3.2.1.1 Hip Abduction/Adduction

Figure 21 illustrates the CAD rendering of the hip actuator. The hip SEA is composed of seven separate parts including the hip, the stoppers, the plungers, the springs, the cable, the two pulleys and the motor and gearbox. Figure 21 does not contain the cable.

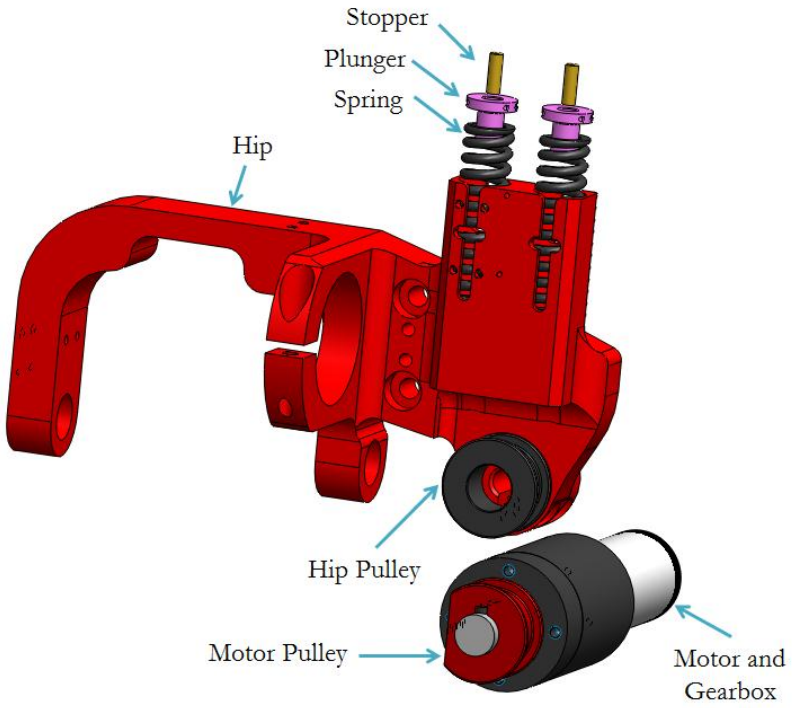

Figure 21: The hip SEA

A cable connects all of these components together. The stoppers crimp onto the cable and are house within the plungers. A knot is also tied at the top of the crimp to lock the cable in place. Likewise, the plungers sit inside the springs which are embedded in the hip structure.

The plungers have a flat bottom which pushes against the flat end of the spring. The cable runs through the center of the plungers, around the hip idler pulley and then to the motor. Once at the motor the cable then completes the opposite path to go to the opposite spring. The cable is also fixed onto the motor pulley to prevent slipping. It should be noted that the hip pulley is resting on an idler and has no rigid attachment to the hip. The only way that power is transmitted to the rotation of the hip is through the springs.

In order to make the actuator work correctly both springs must initially be pre-compressed halfway as shown in Figure 22 . This allows for the series elastic element to work equally in either direction.

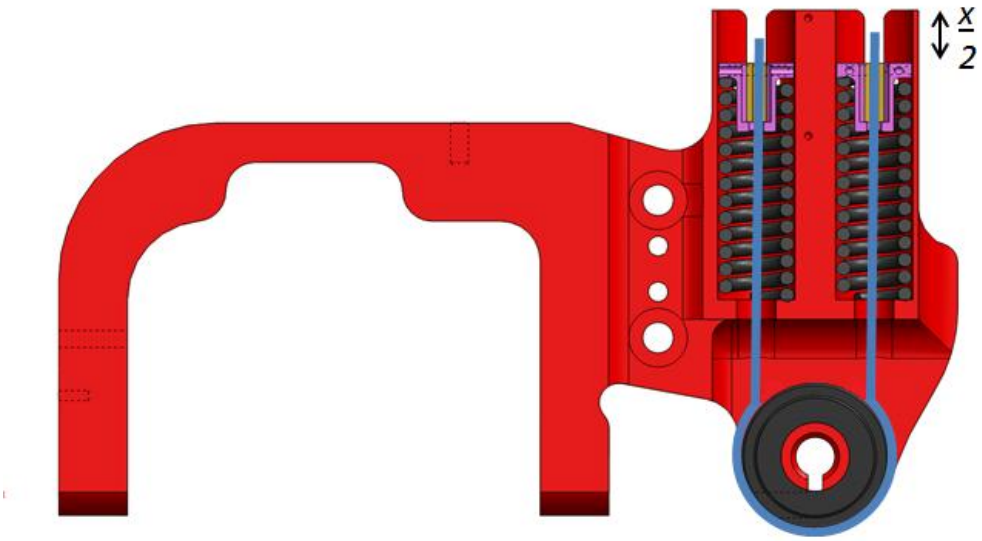

Figure 22: Cutaway section view of the springs inside the hip joint.

In this case the torque of the motor is applied directly to the springs and can be calculated using Equation (33).

$$T_m = R(F_1 - F_2) \tag{33}$$

where R is the radius of the pulley, and F_1 and F_2 are the forces on the two springs. Since the force on each spring is denoted as shown in Equation (34) and the linear displacement of the rotary joint is presented as shown in Equation (35).

$$F = k(x_1 + x_2) \tag{34}$$

$$x_2 = R\theta \tag{35}$$

Using Equations (33), (34), and (35) the output torque can now be calculated as shown in (36)

$$T_0 = 2k\theta R^2 \tag{36}$$

Using Equation (36) the system can control the force intended to be put on the joint.

Because of sudden impulses and external forces, the springs may compress in one of the two allotted directions. Given that the spring is pre-compressed halfway, the max compression of either spring is x. The extreme position of both respective springs can be seen in Figure 23.

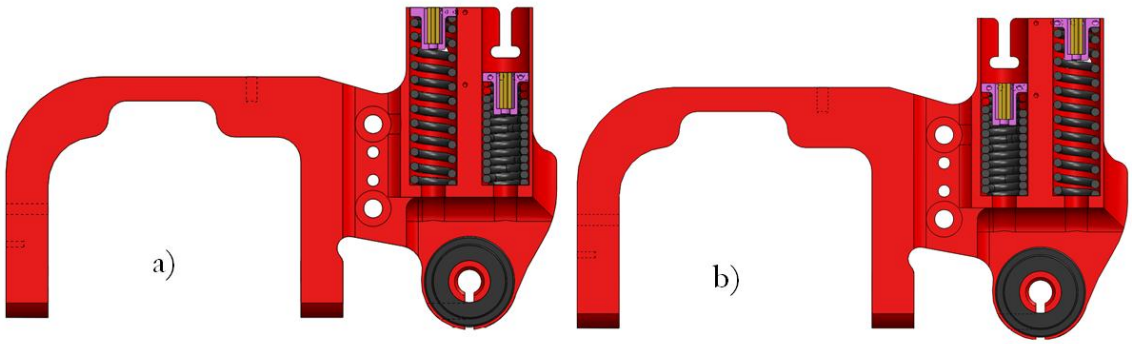

Figure 23: Cutaway of the hip SEA showing springs fully compressed and elongated.

3.2.1.2 Hip Flexion/Extension

The hip flexion/extension uses a very similar system of cleanly integrating the springs directly into the leg structure. Figure 24 illustrates a simplified CAD model of the hip flexion/extension SEA. The general concept behind the implementation of this joint is very similar to the first hip joint. The big change is the addition of two pusher plates screwed together with 0-80 screws on either side of the joint. The spring applies force against these joints to allow the lower leg joint to pivot about the hip joint. It is necessary to have these additional pusher plates in order to make the assembly of the SEA simpler and to keep the overall size of the upper leg joint small. The final product is a neatly integrated SEA directly into the leg link.

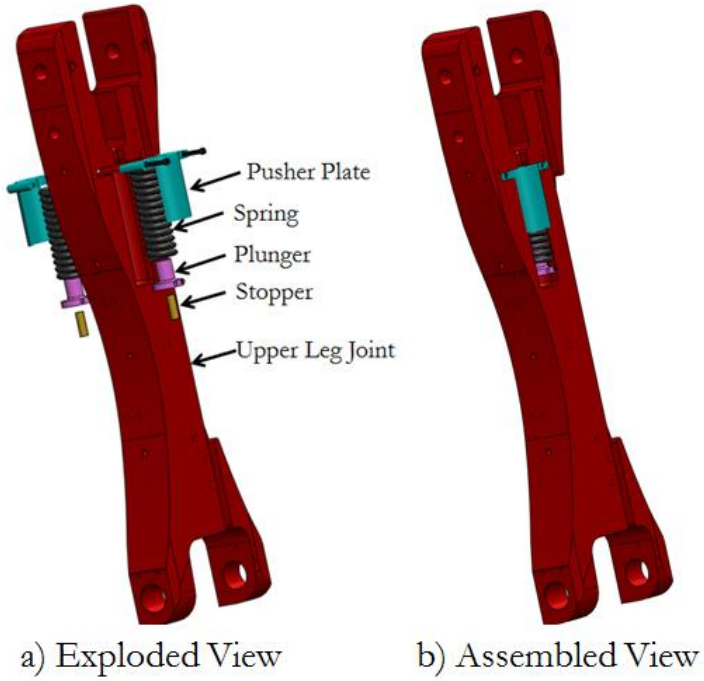

Figure 24: Hip flexion/extension SEA

3.2.1.3 Knee Flexion/Extension

The knee flexion/extension SEA has an almost identical implementation to the hip flexion/extension SEA. There are two pusher plates, two springs, two plungers, and two

stoppers. The only differences are the pusher plates, and which joint this motion controls. The pusher plates must accommodate the varying size of the new joint. An up-close picture depicting the spring integration can be seen in Figure 25.

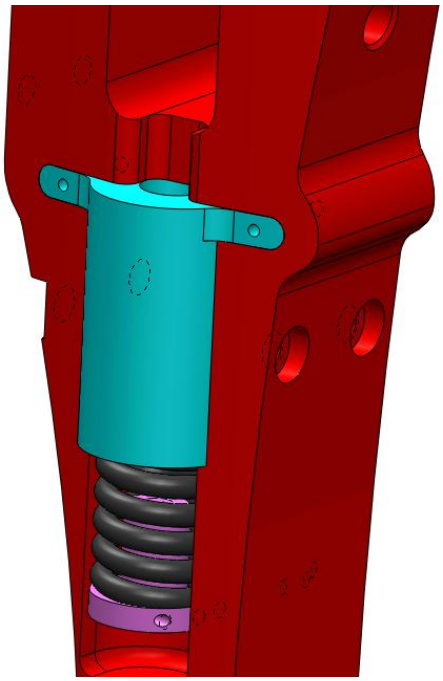

Figure 25: A close up view of Knee Flexion/Extension SEA.

3.2.1.4 Ankle Flexion/Extension

The ankle flexion/extension SEA proved to be one of the more complex to both design and integrate cleanly. The basic integration behind the ankle flexion/extension SEA is very similar to all the other joints. There are again the same stoppers, plungers, and half compressed springs. Figure 26 shows a section view of the ankle flexion/extension joint depicting how the springs, plungers, and stoppers are integrated into the design.

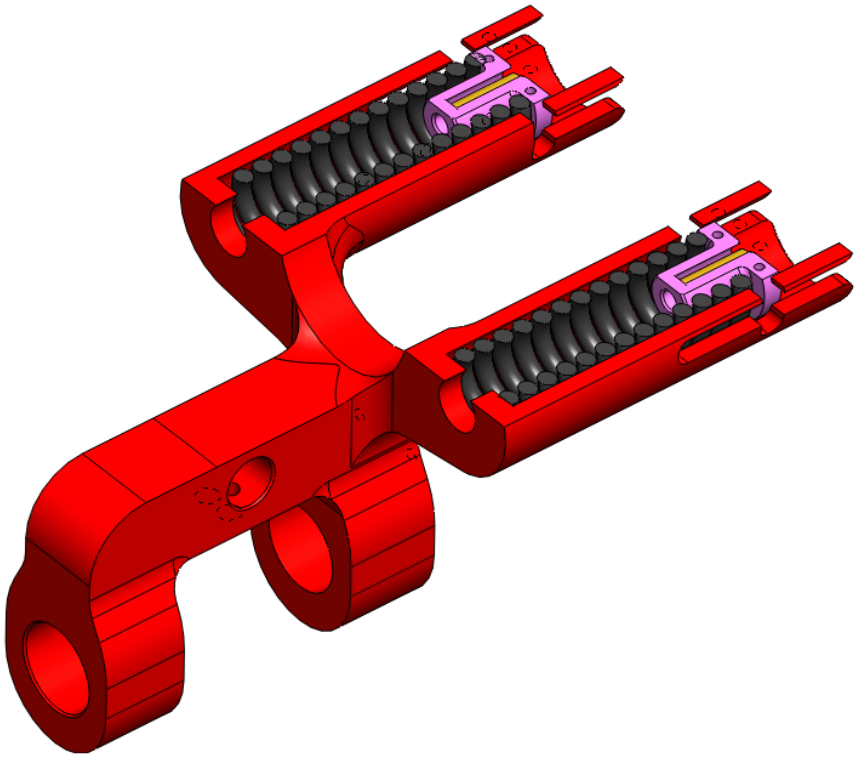

Figure 26: Cutaway view of the ankle flexion/extension SEA

3.2.1.5 Ankle Abduction/Adduction

Similar to all the previously mentioned joints, the ankle abduction/adduction SEA, shown in Figure 28, integrates springs directly into the moving portion of the system. There are two stoppers, two plungers, and two springs all tensioned together with one cable. The one unique aspect of the ankle system is the method in which the cable wraps around, to allow the force pulling on the springs in the flexion/extension axis to causes a rotation in the abduction/adduction plane. Further explanation of the cabling will be provided in Section 3.2.2. This joint can use much weaker springs than the previous four joints due to the lower forces associated with it.

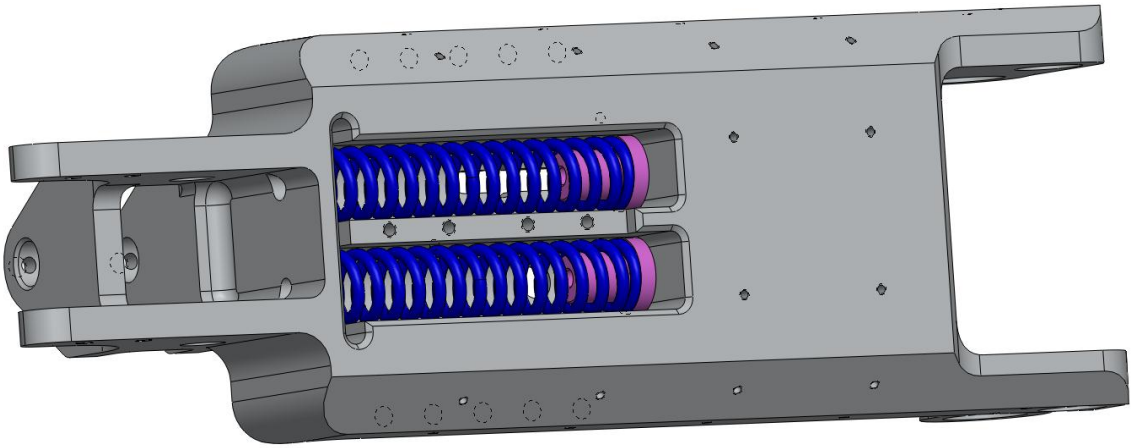

Figure 27: The ankle joint abduction/adduction SEA.

3.2.1.6 Big Toe Abduction/Adduction

The final joint uses a very similar method of integrating springs directly into the design. This joint is one of the more simple ones with a very clean integration of the springs directly into the big toe. The big toe joint again uses even weaker springs than the previous five due to the lower forces. Figure 28 illustrates a cross section view of the big toe SEA.

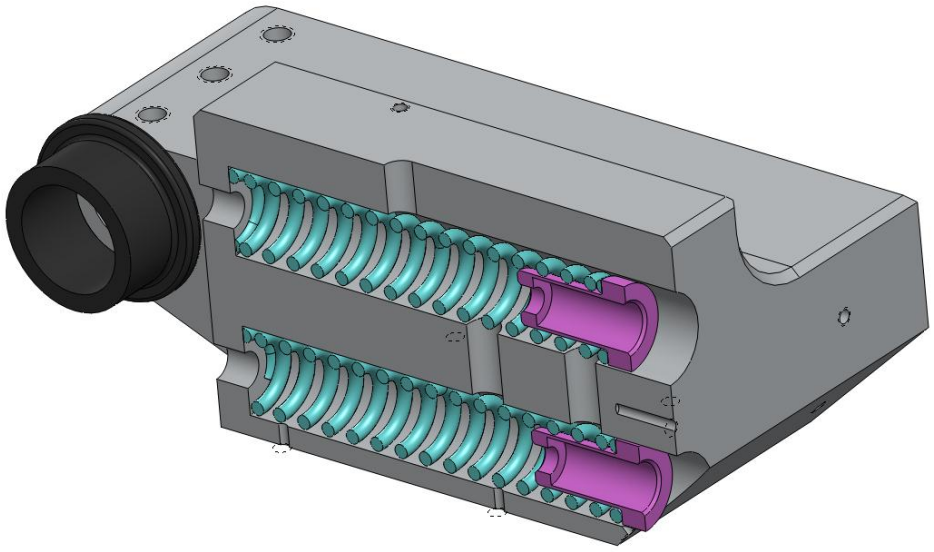

Figure 28: The big toe abduction/adduction SEA.

3.2.1.7 Motor and Spring Selection

Actuators and springs were selected to have adequate properties for the given design. The actuators had to be quick enough to respond to unforeseen disturbances yet still contain enough torque to respond to worst case dynamic forces. Using the dynamic simulation, worst case scenario torques were analyzed and a motor of the proper torque was selected. Motors with good dynamic properties (high acceleration rates and good jerk response) were considered a requirement for the selection process.

Maxon brushless 4 pole motors were selected for the upper four joints due to their high torque, high acceleration response and high power density. The 4 pole technology enabled the use of compact 90 watt motors. Brushless motors of the same size containing 2 poles would only provide for 25 watts of power. The 36 volt winding version of the motor was chosen to keep the current draw low. The final selected motors have a nominal power of 90W, no load speed of 16200 rpm, nominal torque of 50.5 mNm, and are 87% efficient. To keep the motor operating at high efficiency and increase the overall torque, a 111:1 high power spur gearbox was coupled with the motor. While a harmonic gearbox would have been a more ideal solution for this application due to its smaller package, lower weight and higher torque abilities, the long lead times were not suitable for this project. The last two joints used more traditional 2 pole 12 watt brushless motors. 4 pole motors could not be sourced in a package this small, so more traditional brushless motors were used for this application. The 12 watt, 36 V, motors have a nominal torque of 11 mNm, no load speed of 11500 rpm, and are 68% efficient. These motors were coupled with a 128:1 spur gearbox. To achieve the right angle connection needed on the big toe, a set of bevel gears were selected to drive the necessary joint. The gears were selected to have the proper mounting distance and have enough torque to withstand sudden impacts.

To complete the actuator design, high density springs were selected. These springs had to be stiff enough to withstand the forces from the motor yet flexible enough to allow for compliance. The theoretical maximum force on the cable running the top four joints was calculated to be 125 lbs. Since it is undesirable to have the spring be fully saturated, it was necessary to find springs which had a full compression load greater than the maximum expected force with a large deflection. Traditional die springs can generally only compress to about 70% of their elongated length. Hence, the uncompressed length of the spring would need to be relatively large to allow for greater compliance. If the springs are too short then there is not enough bandwidth in the mechanical system to accurately monitor and adjust the force present in the system. Given that 0.75" diameter pulleys were used, a half revolution (or half the circumference of the pulley) would equate to 1.2" of deflection in the cable. While this level of compliance would be desirable it is not realistic in a system of this size. A 138 lb/in, 2" initial length spring was selected for the design. This spring would allow for 50 degrees of compliant interaction on either side of the actuator (under no load). Similar methods were used for the bottom two joints resulting in springs with 35.4 lb/in and 26.8 lb/in restoring forces selected for the ankle joint and big toe joint respectively. The difference in the bottom two springs was chosen simply to better integrate with the design.

3.2.2 Cable System

Cabling the transmission mechanism proved to be one of the most complex parts of the entire assembly. The difficulties resulted due to the tight work space, small tools, and high force springs which needed to be pre compressed halfway on both ends. This section will describe the difficulties for each joint as well, the modifications needed to make the cable system more robust, and the general method used to pre-compress both the springs to the halfway position.

3.2.2.1 Pre-Compressing Springs

In order to allow for the SEAs to work in both directions the springs integrated into the system would all need to be pre-compressed. Hence, when the motor is idle the springs on either side of the pulley oppose one another and are compressed to the midpoint between their elongated length and fully saturated length. This proved to be quite a challenge due to the small workspace and high energy density of the springs. As mentioned in Section 3.2.1.7 Motor and Spring Selection, the three sets of springs were rated at 138lb/in, 39.5lb/in and 38.2lb/in. Given that each spring compresses about 1 inch to reach full saturation this would correspond to approximately 69lb, 20lb and 19lb of force respectively which would need to be applied directly to the spring in order to compress it to the halfway position.

The initial plan to compress the springs was to simply compress each spring halfway and lock it in place with the help of a pin as shown in Figure 29. After a few attempts of half compressing the springs and locking them into the frame, it was clearly seen that this would not be a viable option. The springs simply required too much force to reach this point of compression. Trying to use alternate methods of compressing the springs to lock them in place such as c-clamps failed due to the small work environment.

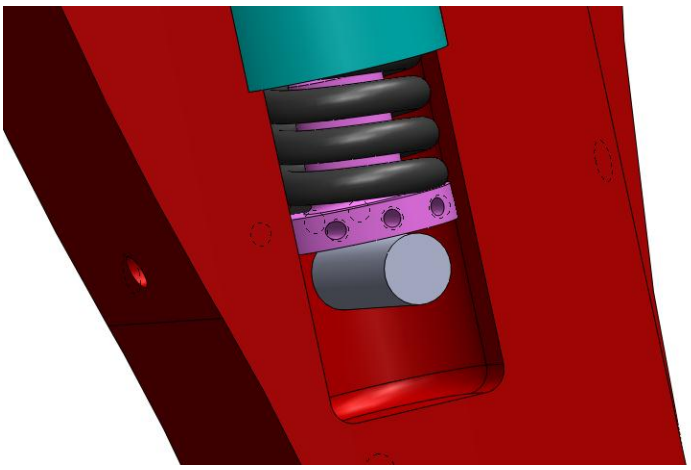

Figure 29: The locking pin for spring pre-compression in upper leg joint.

After realizing that the initial method of pre-compressing both sides would not work, a new method of compressing the springs was developed that involved using the motor to fully compress one spring. The full methodology for pre-compressing and cabling one joint is outlined below.

1. Thread pusher plate, spring, and plunger through the selected cable.
2. Crimp one stopper onto the end of the cable and make a knot in the cable at the end of the crimp. Note that crimping onto the cable is an extra measure of security. In many cases, crimping was omitted due to difficulties in being able to crimp in the given workspace. To date no issues have resulted from not crimping.
3. Wind cable around half of the pulleys, holding all mechanical components in the correct position.
4. Terminate cable at the motor and lock in place.
5. Lock ground element and moving element (e.g. hip and upper leg) together using a c-clamp or other mechanical connection. In some cases, it is advantageous to use a hard stop already implemented into the design such as the knee locking mechanism.

This step makes it such that the ends of the system are both ground and the spring extends without moving either end.

6. Using position control on the motors, wind the spring until it is fully compressed. In the case of the hip abduction/adduction and big toe joints, current control is an easier solution then position control. Current control allows for direct compression of the springs to an exact length.
7. Finish winding the opposite side pulleys.
8. Thread remaining mechanical components and crimp other stopper onto the cable. Additionally tie a knot at the end of the crimp.
9. Release power on motor. The system should be perfectly balanced on both sides.

This method, while very effective, also has difficulties associated with it. Cutting and crimping the cable while the motor is holding position and the spring is fully compressed is a difficult challenge due to the small work environment. Ensuring that all the cables are properly spaced, not overlapping and staying on their desired path is also a challenge. Finally, the entire process has a time limit. In order to keep tension on the high energy springs, the motor is required to put out a lot of force and hold that position. The motor gets very warm if left in this position for an extended period of time and may burnout. To allow for a little extra time, a small muffin fan was used to cool the motor during the spring compression operation. While this process may seem difficult, with enough practice it becomes routine and relatively simple to complete.

3.2.2.2 Cable Selection

Many cables and cable constructions were extensively tested for the purpose of this bipedal robot. Three primary types of cable technologies were extensively explored including

steel cable, vectran cable and dyneema cable. Traditionally, transmission systems involving cables use steel wire rope [12], [44]. Steel wire rope is advantageous due to its high strength and proven robustness even in harsh environments. However, recently many new wire rope technologies have come about. Specifically, vectran and dyneema cable have emerged as serious competitors to steel cable. These two cables are commonly found in marine applications and used as parachute cord. Both of these cables are advantageous due to their high flexibility, low weight, low elongation, low cost and higher rated yield strength. Dyneema, as opposed to vectran, has a higher rated yield strength and is far more slippery. The slippery is advantageous for many joints allowing for lower overall friction in the system. The other advantage to these two cables is the ability to tie knots in order to terminate at pulleys. Overall both the vectran and dyneema cable are much easier to work with. Steel wire rope also comes in a wide variety of strands. Only the 7x19 wire rope was investigated due to its much higher flexibility compared to other strand varieties. The 7x19 wire rope also offers much higher yield strength relative to its other steel wire rope counterparts. Likewise, dyneema also comes in a variety configurations. Only Dyneema SK75 12 strand cable was investigated due to its more robust construction and higher yield strength designed for applications similar to these.

It should also be noted that all investigated steel wire rope also contained a coating on the outside of the strands. While the coating substantially increases the cost of the steel wire rope, it was a necessary choice to ensure the safety of the wire rope. Table 4 illustrates the four heavily investigated wire rope technologies for this robot. After testing, it was found that the 1mm dyneema and the 1.2mm vectran cable were not a feasible solution for this task. The cable consistently broke at a force of roughly 50lb and 40lb, respectively, well under the rated yield strength and the required operational strength of the robot. The cables

broke when trying to pull on the spring. Knowing the deflection the spring endured before the cable breaking it was possible to directly measure the force on the cable. It should be noted that when pulling on the cable it did not break at the crimp or the knot but in the middle. Hence, this is the true yield strength of the wire rope and the crimp and knot are not affecting the operational load of the rope. Based on these results, 1.6mm Dyneema SK75 12 strand cable was chosen as the primary wire rope transmission mechanism for this bipedal robot.

Table 4: Wire rope technologies

Cable	Vendor	Diameter (mm)	Cost/foot	Rated Yield (lb)	Tested Yield (lb)
Dyneema	Yu Wei	1.0	$0.05	250	50
Vectran	Amazon Reseller	1.2	$0.41	220lb	40
7x19 Wire Rope	McMaster	1.6	$1.45	260lb	N/A
Dyneema	R&W Rope	1.6	$0.24	400lb	N/A

3.2.2.3 Cable Routing

Each joint had its own unique design when choosing how to cable the robot. One of the greatest advantages of using cables is the ability to put the motors in any location in any plane. The downside is that the cabling becomes much more difficult as the motors are placed in various planes and various locations. Figure 30 illustrates the routing for the major trivial joints of the system: the hip joint and the big toe joint. As can be seen, these joints are all planar and require a few wraps on each pulley. It should be noted that every pulley requires at least three wraps to provide the proper amount of friction to allow the mechanism to spin. This is especially important on the motor pulley which is required to rotate with the cable to ensure that the system does not slip. While none of the controls are

based on the position of any of the pulleys, the system would respond poorly if slipping was present in the system. This adds another design constraint to the level of robustness that is expected from the cable system. The triple wrapping on every pulley becomes especially important in the more complex joints such as the knee. Tests were conducted simply using one wrap on the cable which resulted in the cable slipping off the joint.

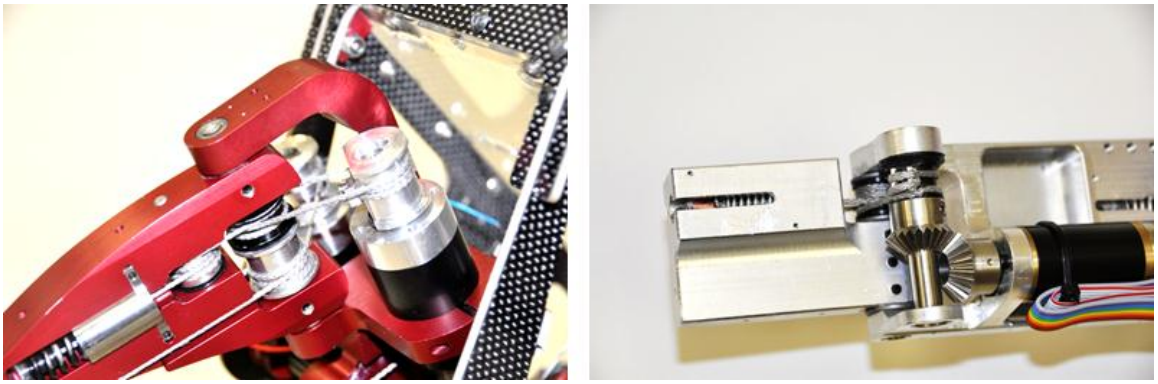

Figure 30: Hip and big toe joint cable routing

The knee joint requires two separate cables to transmit force to the leg. Since the motor is mounted to the hip, an idler pulley is required and mounted at the same location as the hip abduction/adduction joint. Hence, the rotation of the second hip joint will not affect the rotation of the knee. The first method of cabling the knee proved to fail due to the cable continually slipping on the pulley. The issue was a result of only doing a single wire wrap on the pulley. Once the cable rotated close to the limits of the joint friction no longer played an effect on holding the cable. Instead, the clamp was the only thing holding down the cable. To fix this issue a new pulley was designed which had two critical features. One of the features forces the cable into a tight slot while the other forces it through a hole on the side of the pulley and then knots around to ensure that the pulley cannot slip relative to the cable. An illustration of the first and final iteration is shown in Figure 31.

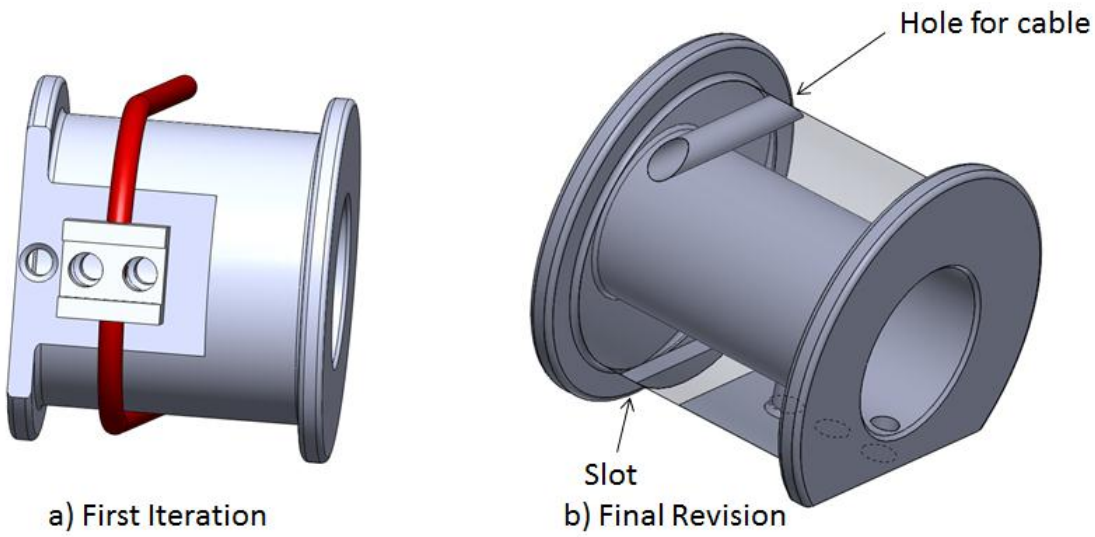

Figure 31: Knee pulley cable wrapping

Since the knee cable had to be terminated at a location without springs it was extremely important to make sure there was plenty of tension on the cable when winding it. Passive tensioners were designed into the system, however they were not advantageous to use due to the increased friction which they would cause in the cable. . Instead a clever method of using the motor to remove all slack in the system was developed. By locking the cable to ground and pulling on the opposite end using the motor it was possible to get the cables very taught and avoid using tensioners. The final cabling for the knee joint is shown in Figure 32.

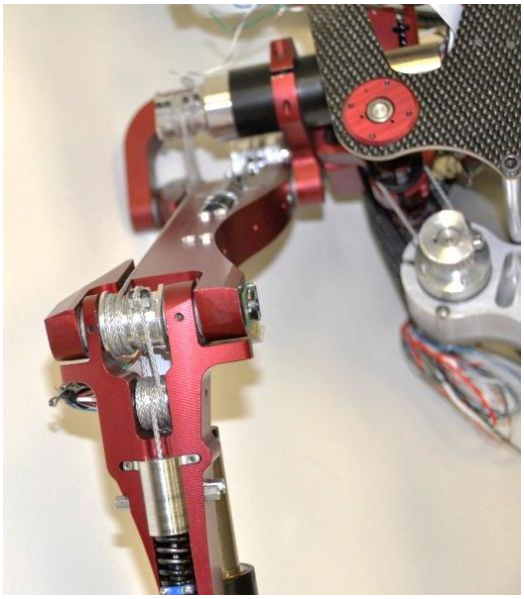

Figure 32: Cabling of the knee joint

The two ankle joints were complex due to the cables having to bend out of plane from their original transmission axis. However, nothing out of the ordinary was necessary to cable these two joints. Similar to all the other joints, a simple termination is needed on the motor followed by winding through a set of pullies and terminating at two springs. The final cabling of the ankle joint is shown in Figure 33.

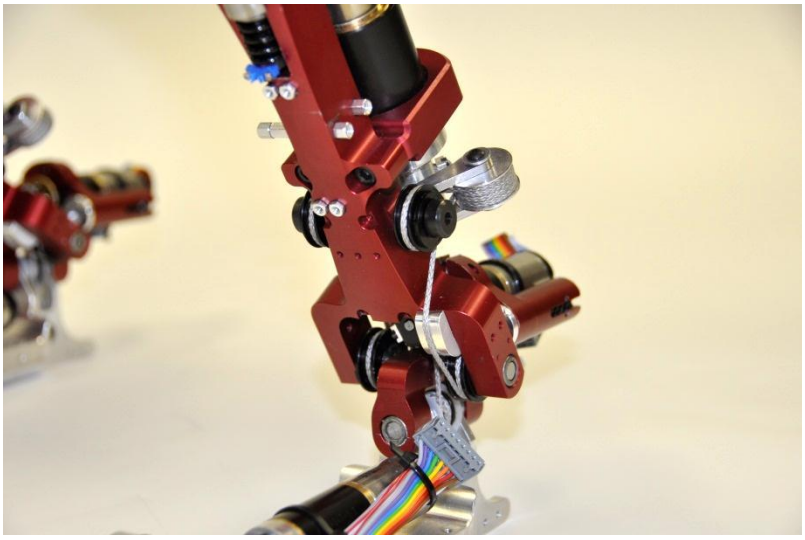

Figure 33: Cabling of the ankle joint.

3.2.3 Stress Analysis of Major Components

One of the project's overarching goals was to create an aesthetically pleasing design which would mimic certain human characteristics. The bone design proved to be very complex needing to suit multiple design constrains in a small package. Each link of the system needed to encapsulate two springs, hold two potentiometers (one linear and one rotary), and accommodate a variety of cables and springs while keeping an aesthetically pleasing appeal. 3D surfacing was heavily used in the leg design process to achieve a more stunning appeal. The leg had to be an appropriate size and shape to accommodate the forces experienced by the system. After a preliminary design was completed, a finite element model for each link of the system was developed to test where the weak point in the system is and ensure that both the bending and stresses associated with the system would not cause any issue with the system. The model calculated both the deformation and safety factor based of Von Mises stresses of each individual link. A 400lb force was applied at the termination point of the cable system (the springs) and a fixed support was placed at the cylindrical location of the joints. A 400lb force was applied since the cable selected for the task had a breaking load of 400lb. While the system is not expected to experience forces of that magnitude, there is no possible way for the system to experience a force greater than 400lb due to the cable being the portion of the system designed to fail first. Figure 34 demonstrates one of the typical outputs seen from the FEA models.

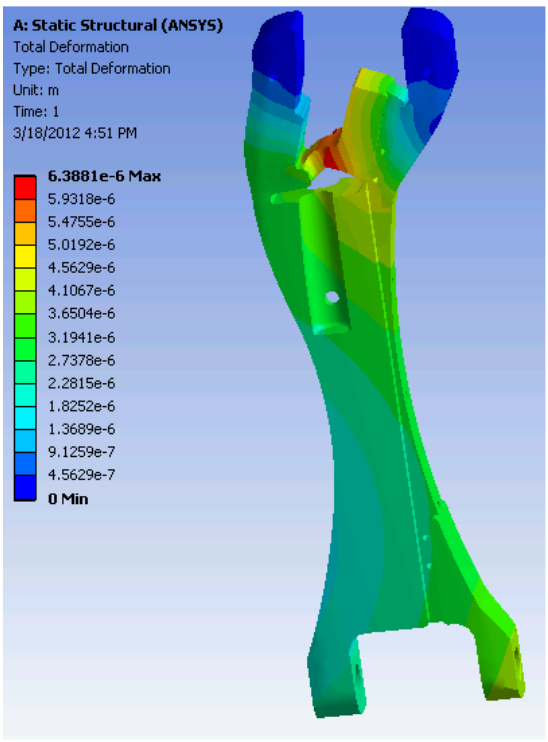

a) Deformation of the top leg

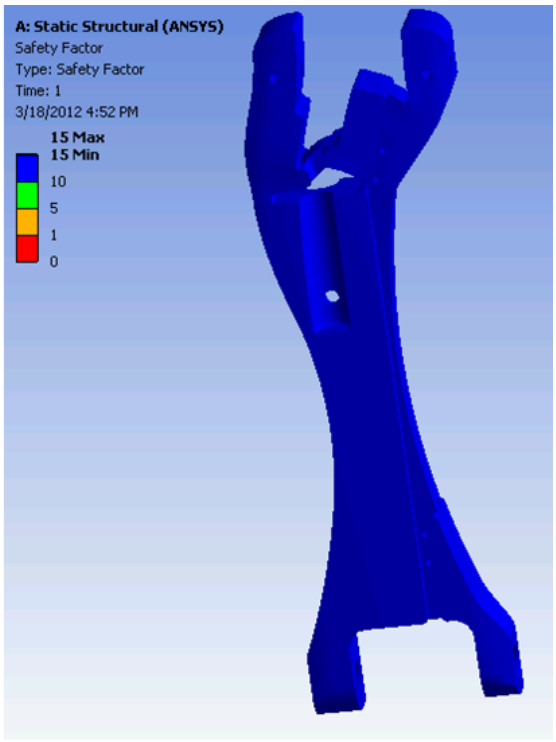

a) Safety factor in the top leg

Figure 34: FEA Model of the top leg of the system.

From Figure 34, the deformation is minimal at only 0.006mm and the safety factor has been computed to be at least 15 at every location. However, not all of the joints have quite as favorable results. Table 5 illustrates the minimum safety factor and max deformation in all of the major joints of the system.

Table 5: Deformation and safety factor of the major joints in the system

Piece	Maximum Deformation (mm)	Minimum Safety Factor
Hip	0.174	4.8
Upper Leg	0.006	15
Lower Leg	0.010	8.7
Ankle	0.542	1.1
Foot	0.356	1.6
Big Toe	0.052	4.6

As can be seen from these results, the ankle has a safety factor which is just barely above 1.0. While being a cause of concern, these are absolute worst case scenarios which are unlikely to ever be seen in the system. As such, the 1.1 safety factor was deemed acceptable and all the desired joints were approved for both functionality and strength. A complete view of all the finite element modeling results can be seen in Appendix D: Finite Element Models.

3.2.4 Passive Locking Knee

The robot successfully implemented a passive locking mechanism for the knee of the robot while simultaneously containing five major degrees of freedom mimicking the major degrees of freedom of a human leg. The knee aids in gait generation and stability of the robot. By designing the robot as a passive dynamic walker the robot is also more efficient while relying on more simplistic behavior. Figure 35 illustrates the locking mechanism in the robot in addition to a few other key components including the placement of the force and position sensors. This locking mechanism has also further proven effective by allowing the robot the ability to stand under its own weight with no power. Due to the locking mechanism the robot can balance in a number of different positions simply using the center of gravity.

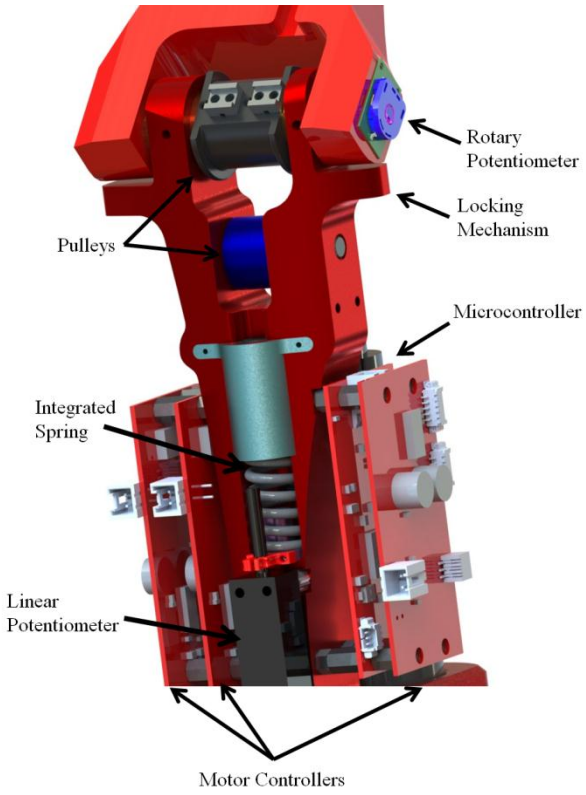

Figure 35: Passive knee locking mechanism

3.2.5 Body Design

The body was designed to hold the main processing unit, the power board of the system, the motor controllers and two large batteries. The body had to hold two motors and contain two pins to act as the ground point for the hip abduction/adduction joint. The overall weight of the body had to be minimized and have an aesthetically pleasing shape. The choice was made to use carbon fiber birch composite for the general shape of the body due to its low weight and high strength. The body was attached used aluminum gusset pieces that were screwed into the carbon fiber frame. The final body with motor mounts, carbon fiber, and aluminum gussets weighed 1.15kg. Adding the motors roughly doubled that weight. A final picture depicting the carbon fiber frame is shown in Figure 36.

a) CAD model

a) Manufactured version

Figure 36: Body design of biped.

The body design required a minor redesign. Upon cabling the hip abduction/adduction joint of the system, the two motors supported by the body began to significantly deflect. The deflection was visible in both the carbon fiber frame as well as the motor to gearbox attachment point. The problem presented a serious issue which required a redesign in the motor attachment mechanism. The other joints supported the actuators by clamping to the gearboxes and not the motors. By clamping to the motors and having such a large cantilevered load there was a large chance of bending a motor, breaking a shaft or seizing a bearing. Instead the choice was made to support the motors with an extended tight fitting tube. The tube would also connect to the carbon fiber and provide the gearboxes with further support. Figure 37 illustrates the proposed new motor connection. It should be noted that in this iteration, the back supports are still used to clamp the motors to the frame. The front supports are guiding tubes which keep the motors perfectly perpendicular to the frame.

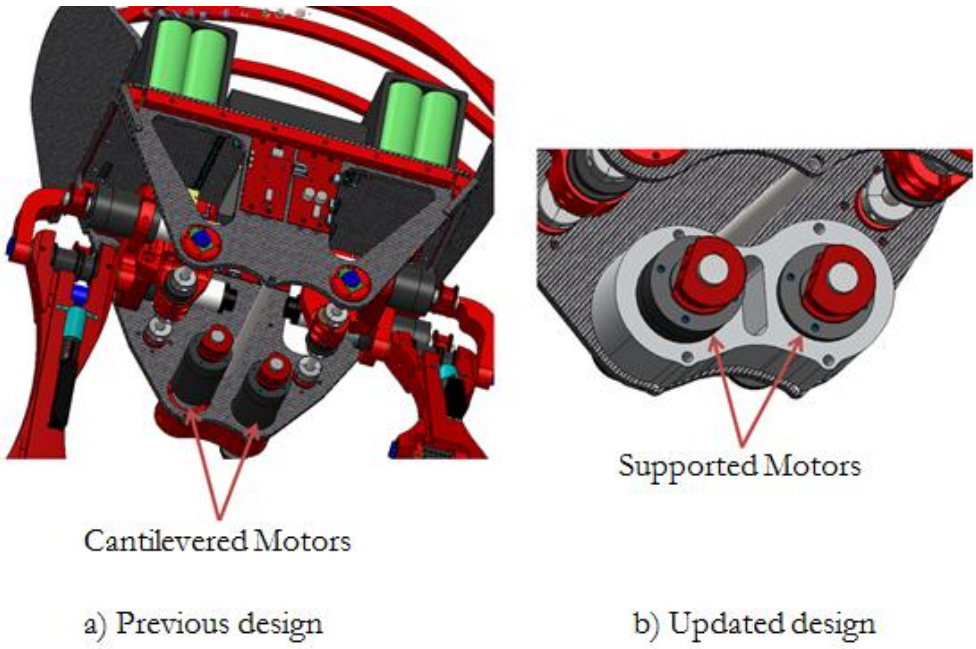

Figure 37: Cantilevered motors and new redesign to better support motors

While the body redesign fixed the issues of the motors and shafts bending, a new problem resulted. Due to the strong connection of the motors to the frame and relatively strong overhung load on the carbon fiber, the entire carbon fiber side was now deflecting with the motors. Another redesign would need to be made in order to make that section stiffer. The solution was to add an additional stiffener on the inner portion of the carbon fiber which would stop deflection. Additionally, the rear mount on the motors was now removed and the front mount was given clamping holes. This change was made to ensure that the motors were not over-constrained. If over-constrained the gearboxes and motors could bend in on themselves and potentially sever the connection point. To ensure that the stiffener plate would fix all the remaining issues, an FEA model was developed to calculate the deflection of a worst case load. It should be noted that no FEA model was developed for the carbon fiber due to the inherent difficulties in modeling a composite material. Figure 38 illustrates the final design of the motor attachment and stiffener plate while Figure 39

illustrates the deformation of the FEA model. As can be seen, in a worst case scenario, the stiffener plate will deflect 1mm. Given that this does not take into account the additional stiffness gained by the carbon fiber, it was determined to be an acceptable amount of deformation.

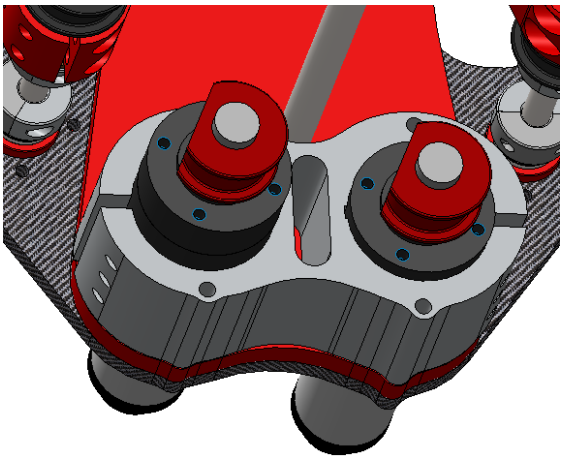

Figure 38: Finalized fixed motor mount design

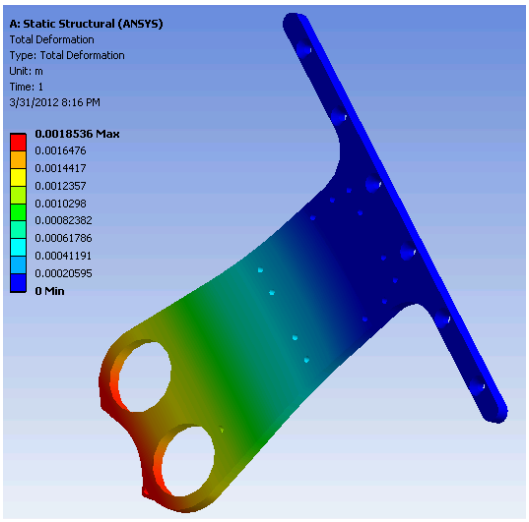

Figure 39: FEA model of stiffener plate

3.2.6 Battery System

A battery system composed of two lithium ion 2300mAh, 36V batteries wired in parallel (for a total of 4060mAh) was mounted atop the robot. Each battery pack consisted of ten 3.6V cells wired in series to form a 36V pack. The battery location was chosen with great care to reduce any affect on the center of gravity of the robot. The low weight of the battery (1.75lbs) also aided in the dynamic characteristics of the robot. The weight of the batteries is 6% of the total weight of the system.

3.2.7 Tactile Sensors

To fully utilize the podotactile feedback, the hardware and the sensor were designed with synergistic considerations. As with biological systems, geometrical placement of sensors along body members directly affects the attainable feedback with regards to sensitivity and

resolution, especially when attached to actuatable limbs. The design of the sensing element is also co-dependent on the movements used to sense contact with the environment. For example, hair along the body provides information regarding motion around the body and compliance in determining proximity to objects due to length while finger print ridges provide roughness information when dragged across a surface. Hence, the design and placement of the sensor and the design and motion of the hardware are codependent. In order to properly implement sensitive walking, the bipedal platform takes the sensor-hardware co-dependence into considerations by encompassing compliant joints, locking knees, an articulated big toe, and podotactile sensors with omnidirectional sensing (shear and normal).

Integrating tactile sensors into the foot design relied on two separate portions: designing a foot to accept printed circuit board/sensors and designing a mold to create the sensors.

3.2.7.1 Tactile Sensor Design

The tactile sensors for this design are hemispherical molded domes designed and tested in Go-Bot [11]. The optical sensors design pictured in Figure 12 have one infrared LED and four phototransistors used to measure the diffracted light in a sensor. The four phototransistors take in light after it has bounced of the molded dome. As the molded dome is pushed on the light will diffract differently and the shear and normal forces will change accordingly. The force applied to the bubble dome can be mapped to phototransistor readings.

3.2.7.2 Designing a Foot and Big Toe

The foot for the robot had to be adequately designed to mount highly compliant tactile sensors onto the foot. The number of sensors is important as well as the location of where they are mounted. To detect how the robot comes in contact with the ground, the choice was made to mount sensors on the bottom of the foot, on the side of the foot as well as at a 45 degree angle relative to the side of the foot. After selecting the size of the components for the sensor, the smallest bubble that could be used was 8mm on the inside diameter and 10mm on the outside diameter. It is advantageous to use smaller sensors such that more accurate force distributions can be attained. These dimensions and constraints then dictated the rest of the foot design.

Similar to the foot, the big toe also needed to be designed with adequate properties. Much like the foot, the big toe needed to have sensors covering the bottom of the toe, the sides of the toe and the 45 degree angle relative to the side of the foot. Additionally, the big toe needed to have sensors on the front of it to allow the robot to sense if it has hit into any object. Again, the size of the bubbles required for the sensors would dictate the overall sizing of the foot. Figure 40 illustrates the final foot design and how the sensors are mounted.

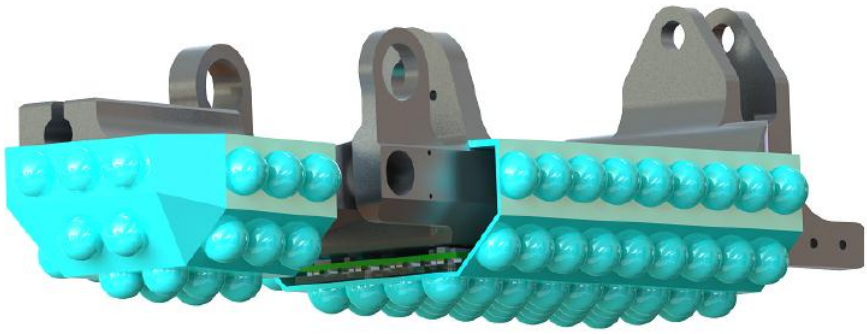

Figure 40: The sensors mounted onto the foot and big toe

3.2.7.3 Designing the Molds

As previously described, the tactile sensors for the feet use hemispherical rubber domes which cover four phototransistors and an infrared LED. The design stems from the sensitive manipulation work completed on the humanoid robot *Obrero* [12]. While the sensors are low cost, they do require custom made molds for any specific application. Freeman V-1062 rubber was selected due to its high tear strength, ease of use and proven record. 3D printing using a fused deposition modeling approach was used to develop negative cavities for the desired mold shape. Multiple iterations were required to ensure that the mold could be easily poured, have few air bubbles and could be easily removed. A six part mold, shown in Figure 41, was designed to allow for pouring the rubber material. The steps in assembling and making the mold are as follows.

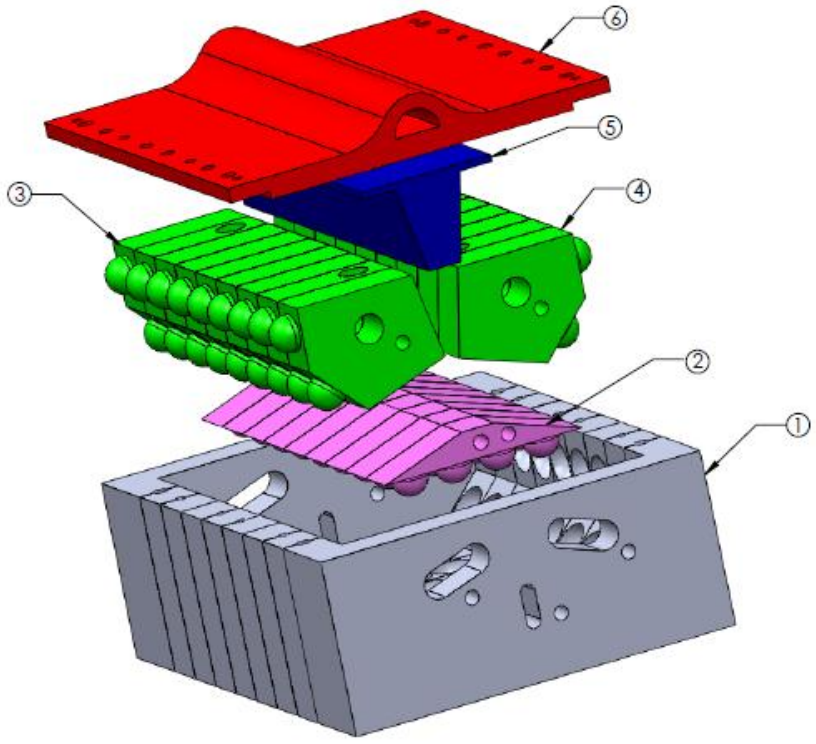

Figure 41: Exploded view of six part mold

1. Mix one part Freeman V-1062 base and 10 part catalyst until the two form a uniform consistency.
2. Put the mix into a vacuum chamber and hold vacuum until all air bubbles have been eradicated. Approximate time should be 20-30 minutes.
3. Pour the solution into piece 1 (base of mold). Great care must be taken that a good consistency is formed when pouring the mold into each individual bubble. The mold must be poured very slowly.
4. Fit piece 2 into position such that there is a thin layer of rubber between piece 2 and piece 1. Piece 2 and piece 1 should now be pinned together in place with 1/8" dowel pins using the holes in the side of both pieces.
5. Vaccum solution one more time. This step is necessary to ensure that no new air bubbles have formed as a result of step 3. If step 3 is performed carefully, the vacuuming should take very little time.
6. Pour a little extra rubber on the sides of the mold.
7. Slide in pieces 3 and 4 and pin into place. Ensure that a little rubber has flowed out on top of pieces 3 and 4
8. Slides pieces 5 and 6 into place and screw entire structure together.
9. Allow structure to settle for 20 hours and then take apart. It should be noted that there are multiple holes and push off screws designed into the structure to allow the mold maker to pull the entire structure apart. Initial iterations lacked these features and the mold would simply be destroyed upon removal.

Using this process, it was possible to create robust molds quickly and effectively. It should be noted that each 3D printed mold was only good for about 2-3 uses before too much residue had been built up and a new mold would need to be made. The residue cannot

be removed without destroying the mold. A final picture of the realized sensor bubbles can be seen in Figure 42.

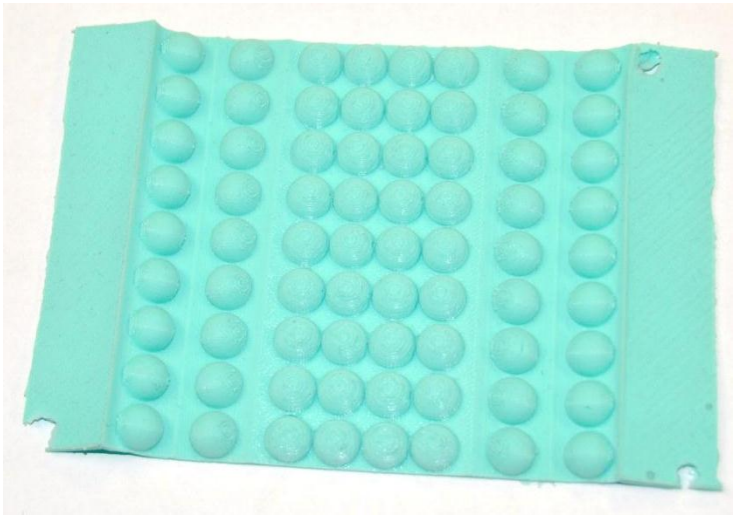

Figure 42: Realized mold

3.3 Electrical Architecture

Figure 43 illustrates an overview of the full electrical architecture of the robot. In this platform, a single on-board computer (FIT PC) is used as the main processing unit. The FIT PC takes in data from a wide array of inputs including the tactile sensor array, the four brushless motor controllers, and the inertial measurement unit (IMU). All of these sensors communicate to the FIT PC over USB. The high data transmission rate of USB is necessary to transmit the required data and quickly respond to the changing terrain seen by the tactile sensor array. The motors are controlled in sets of three by an LPC2148 microcontroller, which reads two potentiometer values per motor and runs a PD controller at 1Khz. This control loop allows the robot to actively balance itself using somatosensory inputs. All of the motor controller and motor drivers are custom designed.

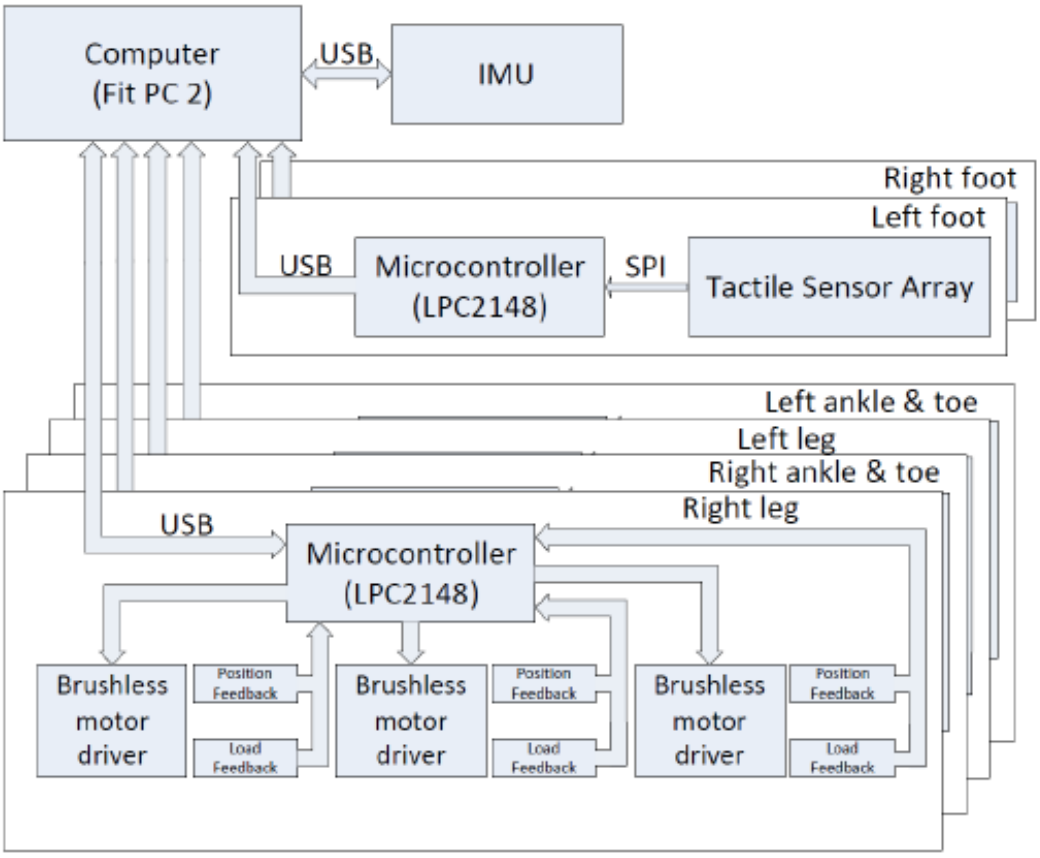

Figure 43: Block diagram of the electronic architecture of the bipedal platform.

To control the SEAs and have fluent leg motion, custom motor controllers capable of handling two position inputs per joint and motion synchronization are used. A system where a single LPC2148 microcontroller controls three motors was integrated into the robot. The LPC2148 microcontroller reads six potentiometers, three for joint position feedback and three for load feedback. The brushless motor drivers allow for simple control of the power output to the motor with a PWM, brake, and direction input. A hierarchical arrangement of controllers is used to better synchronize motion between the motors. In this robot, the top 3 joints are synchronized together and the bottom three are separately synchronized. The top motors control position of the legs and the body while the bottom motors control the orientation.

3.3.1.1 Tactile Sensor Integration

Each foot of the bipedal robot contains a 95 sensor matrix that is sampled at 100Hz using 8 bit analog to digital converters. These sensors are placed on the sole of the foot, at a 45 degree angle to the bottom of the foot and at a perpendicular angle to the foot. Additional sensors are placed on the big toe fully encapsulating the sides and bottom. A microcontroller continually collects all the sensor samples using SPI and sends the data to the main controller, a FIT PC, over USB. The FIT PC receives 1.2 Mb of data from the tactile sensors every second.

The robot's feet are equipped with 190 tactile sensors able to measure force in the normal and shear planes. Each tactile board contains one sensor composed of four transistors and one infrared LED. These sensors have been developed but still require further calibration to equate light sensing into force reading. Figure 44 illustrates the top side of the final tactile sensor board for the bottom of the feet.

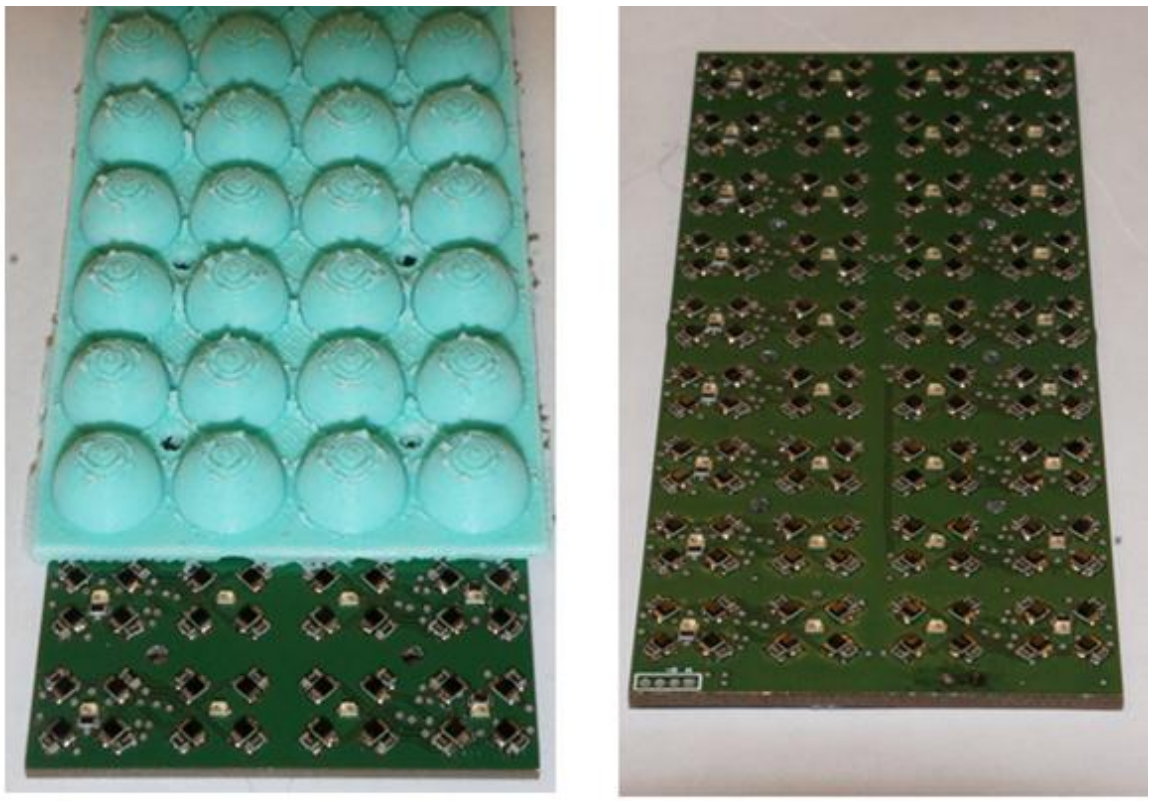

a) Bubbles covering sensors b) Bare sensors

Figure 44: Tactile sensor board.

Chapter 4 Sensitive Walking Algorithms

This section further addresses the implementation of sensitive walking, an approach to robotic walking which expands on sensitive manipulation. With sensitive walking, real-time foot contact feedback is used to perform most of the actions necessary to make the robot walk and maintain stability.

4.1 Traditional Walk

Figure 45 shows an implementation of a robot taking a stride using sensitive walking. In general, as a person's foot comes into contact with the ground, a pressure map of the contact area is generated and the effects of friction, or lack thereof, are sensed. In scene 1 of Figure 45, as the foot is lifted off of the ground, the pressure rolls from the heel, to the balls of the foot, and eventually off of the tip of the toe.

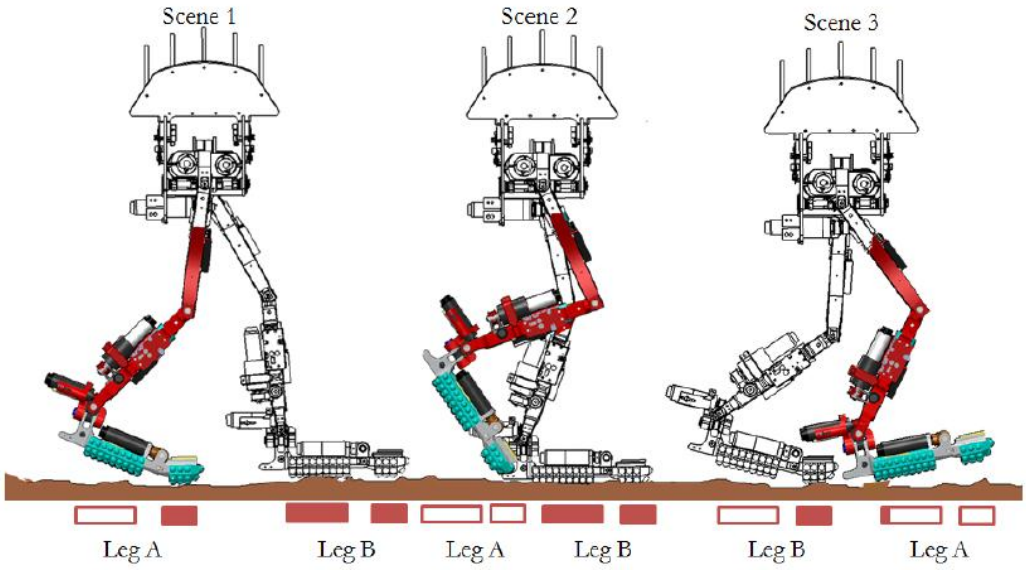

Figure 45: The bipedal robot using sensitive walking to traverse a stair.

Doing so, not only provides dynamic feedback by monitoring the time distribution of the pressure and shear contact but also allows for minute control of the gait. Hence, sensitive walking requires podotactile sensors that reliably detect normal and shear forces generated by the contact with the terrain. It is also assumed that the robot's foot can safely come in contact with the ground using compliant joints. Joint compliance, in general, reduces the required controllable precision in position.

The stages needed to control the steps can be determined using contact feedback. For instance, to begin walking, a robot standing balanced with straight legs needs to shift the balance to one leg while lifting the other. The force distribution on the standing leg will be detected independently of the geometry of the surface where the leg stands, which cannot be done with only four contact points [3]. More importantly, the robot will be capable of detecting when the tip of the toe is the only support point of the rising leg, shown in scene 2 of Figure 45. At that point, the robot will quickly swing the leg forward. The control will determine that the leg is on the air since no ground contact is detected. The tactile feedback on the other foot will confirm that there is no slippage and that the center of mass is moving in a trajectory that avoids instability. The ankle of the standing leg will rotate forward to help the shifting of the body mass. In scene 3 of Figure 2, the landing of the leg will be confirmed by contact and handled through joint compliance. Therefore, precise positioning of the leg is not needed, only a general understanding of the foot location relative to the body is required. This is similar to exploration tasks performed in manipulation.

The geometry of the surface where the foot landed can be evaluated to determine if the next step can be taken. For example, if the foot has landed on the edge of the stair step, the foot should be repositioned. Podotactile feedback also allows the robot to deal with unexpected collisions during leg movements. More complex exploratory behaviors and force

distribution can be done based on the task needs. As an extreme example consider, a person walking on a rope. Focus is placed on balance and placement of the rope directly along the center axis of the foot instead of a pressure distribution. Moreover, the behaviors can be extended to use the feet in scenarios like climbing, or kicking an object. Sensitive walking builds on the wealth of work developed for walking robots where important principles have been developed. The podotactile feedback expands the capabilities of the previous work.

Traditionally, legged gaits for robotic systems have been generated using a combination of biomimetics, ZMP control and path planning. With the use of additional tactile sensors the overall gait generation for the robot when walking on a flat surface has been simplified while simultaneously keeping the system more balanced.

For simplicity we will denote the two legs as leg A and leg B. In the situation of a traditional walk the robot begins by lifting leg A a little of the ground. As leg A is lifted, the robot begins to shift all the weight of the system to leg B. The controller applies the necessary torque to the ankle joints of leg B such that the pressure distribution in the leg is even across the entire foot. As this is going on, the robot continues to lift leg A. Only the hip flexion/extension joint and the knee joint are doing any work in this case. The hip flexion/extension joint is responsible for lifting the leg while the knee joint is responsible for keeping the foot parallel to the ground. Once Leg A has been raised to a sufficient height, the hip flexion/extension joint stops moving the leg up. Now the knee joint of Leg A extends out until the locking element has been reached. Next, Leg B begins to shift its weight to the front until eventually all of the weight has been redistributed to the big toe. As all the weight reaches the big toe of Leg B, simultaneously Leg A should come in contact with the ground. The body of the system should now be located directly above Leg B. The

process is now repeated for however many steps are needed. Figure 46 illustrates the process completed by a person.

Figure 46: Sensitive walking algorithm applied to a traditional walk.

4.2 Traversal of a Step

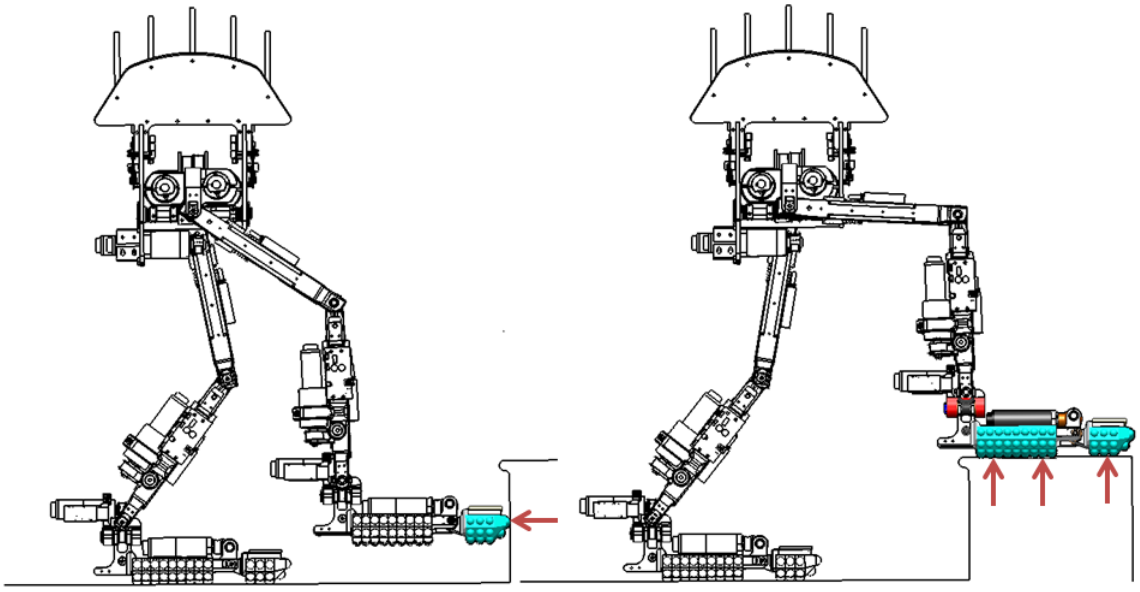

Figure 47: The bipedal robot using sensitive walking to traverse a stair.

A complex, yet common scenario, is the traversal of a step while attempting to ascend either stairs or a sidewalk. Figure 47 depicts the required robot control contact while ascending a step using sensitive walking without a predetermined gait. The flowchart shown in Figure 48 provides a visual of the necessary robot control actions to ascend the step.

Throughout the motion, the podotactile sensors are continuously monitored and processed for balance and stability control. With the robot standing balanced facing the step, the algorithm enters the method through the start block of the flowchart in Figure 48. The robot begins by lifting a foot off of the ground as shown in Figure 47. As the robot's foot comes off the ground, data is immediately relayed from the tactile sensors showing that the system can detect the transition from two feet in contact with the ground down to just one. While the leg steps off the ground, the sensors on the grounded leg provide feedback to

maintain balance on the leg in contact with the ground. Concurrently, the sensors on the floating leg are actively checking to make sure the leg has not bumped into an object as indicated by the loop.

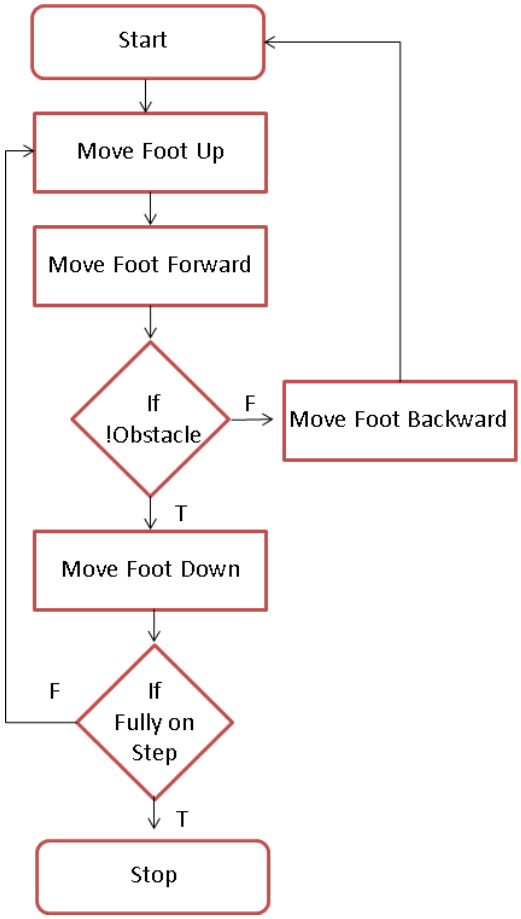

Figure 48: Flowchart for taking a step using sensitive walking.

As the foot approaches the step, the big toe may come in contact with the step in front of it as shown in the first scene of Figure 47. Because of the SEAs, the system is not worried about precisely contacting but rather gracefully complies under contact with the step in front of it. The robot will recognize the stair ahead of it and move the leg up to avoid the step as indicated by the initial loop in the flowchart. If desired, the proprioception sensory and contact information can be used to generate a map of the obstacle. The foot is brought back slightly, until it loses contact with the obstacle, and re-iterates the move up, and forward

motion until no obstacle is detected. Next, the foot is brought down and the sensors are used to verify that the robot is stable in that particular configuration. If the foot sensors do not detect completely placement, then the foot is repositioned as indicated by the second loop in the flowchart. Additionally, the sensors monitor to see if the foot is slipping off the stair and if enough sensors are in contact with the ground. Finally, as the foot comes to the ground the feedback from the tactile sensors is used to redistribute the weight over both legs. Balancing is continuously adjusted while the robot is operational in the same manner than humans innately adjust balance without full cognitive consideration.

Chapter 5 System Validation

This bipedal robot developed for sensitive walking had a number of requirements which would define its success. As a whole, the system met the overall goals by implementing the following key design solutions.

5.1 Design for Sensitive Walking

This bipedal robot was designed for sensitive walking – walking with the help of tactile feedback in unstructured environments. The sensors and limbs of the robots are designed with specific properties in mind ensuring that contact can be made with the ground. Each foot is lined with 190 highly compliant tactile sensors designed to sense precise pressure distributions in each foot.

5.2 Design with a Locking Knee

As described, the robot employs a passive locking knee mechanism. The mechanism allows the robot to walk with a higher efficiency and more inherent stability and control. The robot may not extend its lower leg past the angle of the upper leg due to the mechanical stop.

5.3 Degrees of Freedom

As previously explained the robot was designed to mimic the major degrees of freedom in a human leg. Each leg contains six degrees of freedom which mimic two rotations in the human hip, one rotation in the human knee, two rotations in the ankle and

one final joint in the big toe. These degrees of freedom correlate directly to a human and allow for the system to have high mobility.

5.4 Mimic Toddler in Size and Height

Requirements included designing the robot around a certain size and weight. The final robot weighs approximately 12kg and stands just shy of 1 meter tall. Hence, the original requirements of the system have been perfectly met. The low overall weight of the system allows the robot the ability to carry larger payloads or walk with a faster gait.

5.5 Integration of Series Elastic Actuators

The robot successfully integrated series elastic actuators into each joint of the system allowing for a greater compliance and the ability to easier control the force in the system. Traditional impedance control calls for a solution to a complex controls problem relying on current sensors to backsense the overall force on the system. However, with series elastics this robot can now sense the exact force being put out at any time directly. The compliance in the system has also been extensively tested through testing holding position on the position of the joint but actively introducing an external force to the system. With the external force it is clear to see a deflection in the spring, however there is no deflection in the position of the joint. Consequentially, the force on the system can be directly measured. Figure 49 illustrates the spring compliance added to the system. In this test the robot's motor was held at a fixed position. At the same time rapid dynamic forces were imposed on the system. The dynamic forces, while visible in the spring, do not translate back to the motor. Figure 49 illustrates two positions of the spring while imposing forces on the system in both directions.

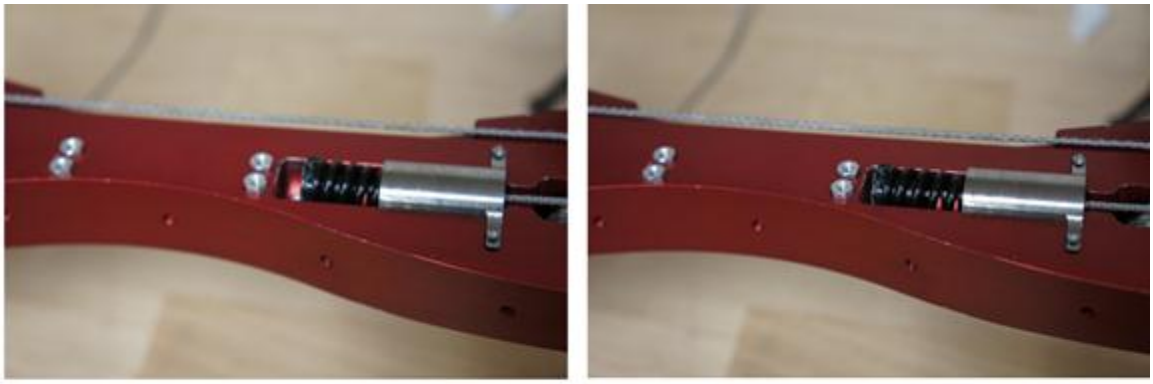

Figure 49: Spring compliance in the system.

5.6 Untethered Control

As stated in the design requirements, the robot must be entirely untethered. As legged robots are designed to handle rough dynamic terrain, developing a biped which can only work under structured environment severely limits its functionality and use. A full power system was also developed for the robot. The robot runs off two lithium ion 2300mAh batteries running at 36 volts wired in parallel. The two batteries due to the lithium ion technology weigh only 1.75lbs. Under typical operation the robot has a theoretical run time of approximately 30 minutes under walking conditions or an hour idle time. Run time calculations assume 25% power performance.

5.7 Overall System Performance

As a whole the full system has been tested on an individual basis. Each joint has been powered and moved to its full extents (recorded in Table 6). Each joint has also extensively been tested for robustness. The springs of every joint have been bottomed out multiple times with no permanent harm imposed on the system. The robot has also collided

into itself on many occasions with no permanent damage. As a whole the robot has been successfully designed to be robust and have the ability to survive minor falls without having to worry about breaking key structural members.

Table 6: Robot joint ranges

Joint	Max Angle	Min Angle
Hip Abduction/Adduction	40º	-30º
Hip Flexion/Extension	95º	-95º
Knee Flexion/Extension	95º	0º
Ankle Flexion/Extension	20º	-60º
Ankle Abduction/Adduction	90º	-90º
Big Toe Flexion/Extension	95º	-20º

Chapter 6 Conclusion and Future Work

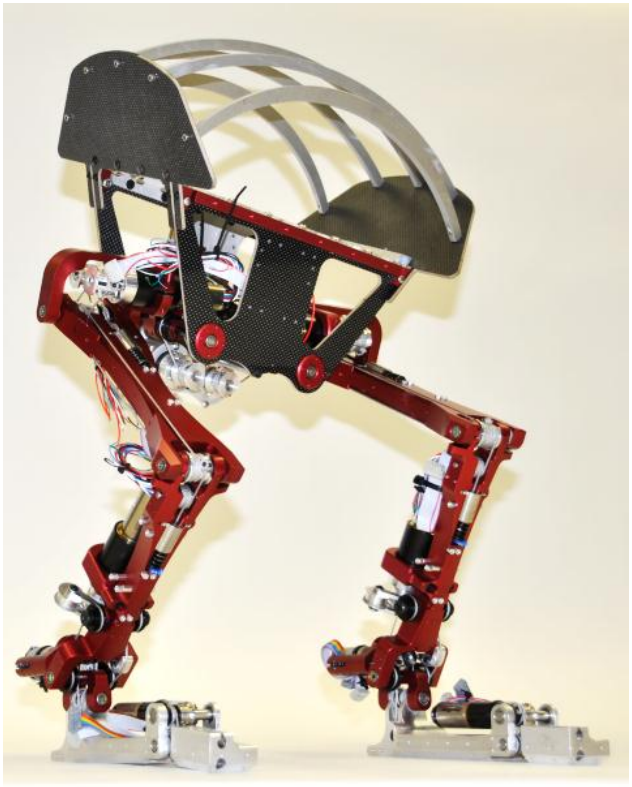

Figure 50: Final bipedal robot

This thesis presented the design of a state-of-the-art bipedal robot, shown in Figure 50, designed for the purpose of sensitive walking. The bipedal robotic platform encompasses twelve SEA-based compliant joints for graceful contact, locking knees to mimic passive dynamics, an actuated big toe for more precise ground contact control and stabilization, and omnidirectional tactile sensors capable of measuring shear and normal forces. The robot consists of 190 highly flexible tactile sensors lining the soles of the feet and big toes. A kinematic and dynamic model was developed for the system. Detailed design considerations including spring and motor selection have also been presented and analyzed. FEA models were developed to ensure structural stability of the system. Finally, sensitive walking algorithms were developed for the purpose of allowing the robot to walk using the additional

somatosensory input. Example algorithms including walking up a set of stairs and walking on a moderately rough terrain have been presented.

While this system has been fully developed and each individual mechanical link has been tested there is still a great amount of work to be completed in developing the sensitive walking algorithms. Preliminary work has been completed on integrating electronics and developing a high level controller for the robot however the work is still at a preliminary stage. More simulation and real life testing is needed to justify the tactile sensors. This research focused mostly on the modeling and mechanical design of a robust system so many elements of the actual sensitive walking have not been fully integrated into the high level control scheme. Immediate tasks for the future should include the following:

- Fully integrate all motor controllers.
- Complete sensor board and mapping of sensor data to computer
- Integrate IMU into control scheme
- Develop more robust simulation which handles controls algorithms. Possible integration with BULLET would be a good solution for a more robust dynamic simulation.
- Develop simpler method of cabling full robot together. In place tensioners would be a good solution. This would allow the robot to be cabled without relying on the motor to compress the springs.

Once all of the electrical and systems programming sections of the project are fully integrated this robot will serve to prove the necessity in integrating podotactile feedback in a walking system.

References

[1] M. Raibert, "Dynamic legged robots for rough terrain" in *10th IEEE-RAS International Conference on Humanoid Robots*, 2010.

[2] R. S. Johansson and G. Westling, "Attention and Performance XIII", chapter Tactile afferent signals in control of precision grip. Lawrence Erilbaum Association., Hillsdale, NJ, 1990.

[3] http://world.honda.com/ASIMO/technology/2011/specification/, Asimo (2011-) Key Specificaitons, (last accessed on the 6th of January, 2012).

[4] M. Popovic, A. Goswami and H. Herr, "Ground reference points in legged locomotion: defenitions, biological trajectories and control implications," in *International Journal of Robotics Research* Vol. 24, No 12. Pp. 1013-1032, 2005.

[5] M. Vukabortovic, H. Herr, B. Borova, M. Rakovic, M. B. Popovic, A. Hoffman, M. Jovanoic, and V. Potkonjak, "Biological principles of control selection for a humanoid robot's dynamic balance preservation," in *International Journal of Humanoid Robotics* Vol. 5, No. 4, pp 639-678, December 2008.

[6] M. Vukobratovic, B. Borovac, "Zero-moment point – thirty five years of its life," in *International Journal of Humanoid Robotics*, Vol. 1, No. 1, pp. 157-173, 2004.

[7] P. Sardain and G. Bessonet, "Forces acting on a biped robot, center of pressure – zero moment point," in *IEEE Trans. Systems, Man and Cybernetics,* Part A. Vol 34, No.5, pp. 630-637, 2004.

[8] A. Dollar, L. Jentoft, J. Gao, and R. Howe. Contact sensing and grasping performance of compliant hands. *Autonomous Robots*, 28:65–75, 2010.

[9] RoboSKIN Project. http://www.roboskin.eu/index.php.

[10] J.M. Romano, K. Hsiao, G. Niemeyer, S. Chitta, and K. J. Kuchenbecker Human-inspired robotic grasp control with tactile sensing. *IEEE Transactions on Robotics*, 27 (6):1067 – 1079, December 2011.

[11] E. Torres-Jara and G. Gomez. Fine sensitive manipulation, in *Australasian Conference on Robotics and Automation,* Canberra, Australia, 3-5 December 2008.

[12] E. Torres-Jara. Sensitive Manipulation. PhD thesis, Massachussets Institute of Technology Computer Science and Artificial Intelligence Laboratory, 32 Vassar Street, Cambridge, MA 02139, 2007.

[13] L. Natale and E. Torres-Jara. A sensitive approach to grasping, in *Proceedings of the sixth international workshop on epigenetic robotics*, pages 87–94, 2006.

[14] M. Raibert, "Legged Robots," *Communications of the ACM*, 499 Vol 29, No. 6, 1986.

[15] http://www.ai.mit.edu/projects/leglab/background/milestones.html, Milestones in the Development of Legged Robots, last accessed on the 5th of January, 2012.

[16] J. Pratt, "Exploiting inherent robustness and natural dynamics in the control of bipedal walking robots," Ph.D. dissertation, Dept. Electrical Engineering and Computer Science, MIT, Boston, MA, 2000.

[17] M. Raibert, K. Blankespoor, G. Bnelson, R. Playter, and the Big-Dog Team, "BigDog, the Rough-Terrain Quadruped Robot," in *Proceeding of the 17th World Congress The Interntaional Federation of Automatic Control (IFAC)*, 2008.

[18] J. Pratt and G. Pratt, "Intuitive control of a planar bipedal walking robot," in *IEEE International Conference on Robotics & Automation*, 1998.

[19] S. Eppinger and W. Seering, "Three dynamic problems in robot force control," in *IEEE International Conference on Robotics and Automation*, pp 392-397, 1989.

[20] S. Eppinger and W. Seering, "Understanding bandwith limitation in robot force control," in *IEEE International Conference on Robotics and Automation*, 1987.

[21] G. Pratt, M. Williamson, P. Dilworth, J. Pratt, K. Ullsand, and A. Wright, "Stiffness isn't everything," in *Proceeding of ISE*R, Stanford, CA, 1995.

[22] J. Yamaguchi, E. Soga, S. Inoue and A. Takanishi, "Development of a bipedal humanoid robot – control method of a whole body cooperative dynamic biped walking," in *IEEE International Conference on Robotics and Automation*, pp. 386-374, 1999.

[23] S. Setiawan, S. Hyon, J. Yamaguchi, and A. Takanishi, "Physical interaction between human and a bipedal humanoid robot – realization of human-follow walking," in *IEEE International Conference on Robotics and Automation*, pp. 361-367, 1999.

[24] Honda Motor Co. Ltd., "Asimo technical information," 2007.

[25] M. Vukobratovic, A. Frank and D. Juricic, "On the stability of biped locomotion,": in *IEEE Trans. Biomedical Engineering.* Vol. BME-17 No. 1, 1970.

[26] A. Takanishi, T. Takeya, H. Karaki, and I. Kato, "A control method for dynamic biped walking under known external force," in *Proc. IEEE Int. Workshop Intelligent Robots and Systems*, pp. 795-801, 1990.

[27] T. McGeer, "Passive dynamic walking," *International Journal of Robotics Research* Vol 9 No 2, pp. 62-82, 1990a.

[28] T. McGeer, "Passive dynamic walking with knees," in *IEEE International Conference on Robotics and Automation*, pp. 1640-1645, 1990b.

[29] K. Byl and R. Tedrake, "Metastable walking machines," *International Journal of Robotics Research*, Vol 28 No 8, pp. 1040-1064, 2009.

[30] K. Byl and R. Tedrake, "Approximate optimal control of thre compass gait on rough terrain," in *IEEE International conference on Robotics and Automation*, 2008.

[31] R. Tedrake, "Applied optimal control for dynamically stable legged locomotion," Ph.D. dissertation, Dept. Electrical Engineering and Computer Science, MIT, Boston, MA, 2004.

[32] S. Collins and A. Ruina, "A bipedal walking robot with efficient and human-like gait," in *IEEE International Conference on Robotics and Automation*, 2005

[33] S. Collins, A. Ruina, R. Tedrake, and M. Wisse, "Efficient bipedal robots based on passive-dynamic walkers," *Science,* Vol 307, February 2005.

[34] R. S. Johansson and R. H. LaMote, "Tactile detection thresholds for a single asperity on an otherwise smooth surface," *Somatosensory Research*, pp. 21-31, 1983.

[35] B.D. Argall and A.G. Billard. A Survey of Tactile Human-Robot Interactions. *Robotics and Autonomous Systems*, 58(10):1159–1176, 2010. ISSN 0921-8890.

[36] H. Ritter, J. Jockusch, and J. Walter. "A tactile sensor system for a three-fingered robot manipulator," in *Int. Conf. on Robotics and Automation*, 1997.

[37] P. Lang. "Design and prototyping of a fibre optic tactile array," *The Journal of High School Science*, November 2002.

[38] B. Siciliano, and O. Khatib, "Force and Tactile Sensors," in *Springer Handbook of Robotics*, 1st ed: Springer, 2008, ch. 19, sec 1.4, pp. 459-470.

[39] M. Raibert, K. Blankespoor, G. Nelson, R. Playter, and the BigDog Team. Bigdog, the rough–terrain quadruped robot. In *Proceedings of the 17th World Congress*, pages 10823–10825, 2008. URL http://www.bostondynamics.com/img/BigDog IFAC Apr-8-2008.pdf.

[40] K. Suwanratchatamanee, M. Matsumoto, and S. Hashimoto. Balance control of robot and human-robot interaction with haptic sensing foots, in *Human System Interactions, 2009. HSI '09. 2nd Conference* on, pages 68 –74, may 2009. doi: 0.1109/HSI.2009.5090956.

[41] http://www.kuka-robotics.com/usa/en/products/software/educational_framework/arm_tutorials/PS_Content_Arm2.htm, KUKA Industrial Robots - Arm Tutorial 2, last accessed on the 25th of February, 2012.

[42] B. Siciliano, and O. Khatib, "Dynamics," in *Springer Handbook of Robotics*, 1st ed: Springer, 2008, ch. 2, sec 2.3-2.6, pp. 43-55.

[43] L. Sentis, M. Slovich, "Motion planning of extreme locomotion maneuvers using multi-contact dynamics and numerical integration," in *Humanoid Robots (Humanoids), 2011 11th IEEE-RAS International Conference,* pp.760-767, 26-28 Oct. 2011

[44] J. Hurst. The Role and Implementation of Compliance in Legged Locomotion. PhD thesis, Carnegie Mellon University Robotics Institute, Pittsburgh, PA, 2008.

Appendix A: Forward Kinematics

```
% This script calculates the forward kinematics of the biped robot
% developed for the Sensitive Robotics Laboratory/Stinger Labs. Both the numerical and
analytical solution have been derived.

%% Initialization Clearing Scripts
clc;
clear all;
close all;

%% Ask user if analytical or numerical
num=input('Would you like the numerical solution? (1 for yes) ');
%% Allocating Space
theta=zeros(1,6);
T=zeros(4,4,11);

%% Define Thetas
if num==1
    theta=[0 0 0 0 0 90]; %Test case pointing straight down
else
    syms theta1 theta2 theta3 theta4 theta5 theta6;
end

%% Define Remaining DH Parameters
a=[0 8.25 8.71 .719 1.36 1];
d=[0 3.06 0 0 5.32 0];

if num==1
    alpha=[90 0 0 -90 90 0];
else
    alpha=[pi/2 0 0 -pi/2 pi 0];
end
%% Creating Matrices

if num==1
%Numerical
    for i=1:6
        T(:,:,i)=[cosd(theta(i)) -sind(theta(i))*cosd(alpha(i))
sind(theta(i))*sind(alpha(i)) a(i)*cosd(theta(i));
            sind(theta(i)) cosd(theta(i))*cosd(alpha(i)) -cosd(theta(i))*sind(alpha(i))
a(i)*sind(theta(i));
            0 sind(alpha(i)) cosd(alpha(i)) d(i);
            0 0 0 1];
    end

else
%Symbolic
A=[cos(theta1) -sin(theta1)*cos(alpha(1)) sin(theta1)*sin(alpha(1)) a(1)*cos(theta1);
        sin(theta1) cos(theta1)*cos(alpha(1)) -cos(theta1)*sin(alpha(1))
a(1)*sin(theta1);
        0 sin(alpha(1)) cos(alpha(1)) d(1);
        0 0 0 1];

B=[cos(theta2) -sin(theta2)*cos(alpha(2)) sin(theta2)*sin(alpha(2)) a(2)*cos(theta2);
        sin(theta2) cos(theta2)*cos(alpha(2)) -cos(theta2)*sin(alpha(2))
a(2)*sin(theta2);
        0 sin(alpha(2)) cos(alpha(2)) d(2);
        0 0 0 1];

C=[cos(theta3) -sin(theta3)*cos(alpha(3)) sin(theta3)*sin(alpha(3)) a(3)*cos(theta3);
        sin(theta3) cos(theta3)*cos(alpha(3)) -cos(theta3)*sin(alpha(3))
a(3)*sin(theta3);
        0 sin(alpha(3)) cos(alpha(3)) d(3);
        0 0 0 1];

D=[cos(theta4) -sin(theta4)*cos(alpha(4)) sin(theta4)*sin(alpha(4)) a(4)*cos(theta4);
```

```
        sin(theta4) cos(theta4)*cos(alpha(4)) -cos(theta4)*sin(alpha(4))
a(4)*sin(theta4);
        0 sin(alpha(4)) cos(alpha(4)) d(4);
        0 0 0 1];

E=[cos(theta5) -sin(theta5)*cos(alpha(5)) sin(theta5)*sin(alpha(5)) a(5)*cos(theta5);
        sin(theta5) cos(theta5)*cos(alpha(5)) -cos(theta5)*sin(alpha(5))
a(5)*sin(theta5);
        0 sin(alpha(5)) cos(alpha(5)) d(5);
        0 0 0 1];

F=[cos(theta6) -sin(theta6)*cos(alpha(6)) sin(theta6)*sin(alpha(6)) a(6)*cos(theta6);
        sin(theta6) cos(theta6)*cos(alpha(6)) -cos(theta6)*sin(alpha(6))
a(6)*sin(theta6);
        0 sin(alpha(6)) cos(alpha(6)) d(6);
        0 0 0 1];

end
%% Multiplication of matrices
if num==1
    %Numerical
    T(:,:,7) = T(:,:,1)*T(:,:,2);
    T(:,:,8) = T(:,:,1)*T(:,:,2)*T(:,:,3);
    T(:,:,9) = T(:,:,1)*T(:,:,2)*T(:,:,3)*T(:,:,4);
    T(:,:,10) = T(:,:,1)*T(:,:,2)*T(:,:,3)*T(:,:,4)*T(:,:,5);
    T(:,:,11) = T(:,:,1)*T(:,:,2)*T(:,:,3)*T(:,:,4)*T(:,:,5)*T(:,:,6);
else
    %Symbolic
    FK1=A*B*C*D*E*F;
    Q=vpa(simplify(FK1),2)
end
%% Extracting XYZ Points for Plotting
if num==1
    Tx(1:5)=T(1,4,7:11); % Extract X
    Ty(1:5)=T(2,4,7:11); % Extract Y
    Tz(1:5)=T(3,4,7:11); % Extract Z
    Txyz=zeros(3,6); % Allocating Space
    Txyz(1:3,2:6)=T(1:3,4,7:11); %Making a Matrix of all 3 positions

    %% Plotting
    plot3(Txyz(1,:),Txyz(2,:),Txyz(3,:),'*-b')
    grid on
    axis equal
    axis on
else
end
```

Appendix B: Inverse Kinematics

```
function [theta1 theta2] = twoLinkInv(x,y,l1,l2)
theta2 = zeros(2,1);
theta2(1) = real(acos((x^2+y^2-l1^2-l2^2)/(2*l1*l2)));
theta2(2) = -theta2(1);
phi = atan2(y,x);
psi = atan2(l2*sin(theta2),l1+l2*cos(theta2));
theta1 = real(phi-psi);
```

```
%Ellipse Model
clear all;
close all;
xh = 0;
yh = .4;
l1 = .21;
l2 = .22;
xs = zeros(101,1);
ys = zeros(101,1);
for t = 100:-1:50
    xht = xh + .1*cos(2*pi/3+pi/6)*(-1*t+100)/100;
    x1 = .2*cos(2*pi/3*t/100+pi/6);
    y1 = .03*sin(2*pi/3*t/100+pi/6)-0.015;
    [theta1 theta2] = twoLinkInv(x1-xh,y1-yh,l1,l2);
    [xe ye] = frameOfRef(l1,l2,theta1,theta2,-xht,yh);
    xs(101-t) = xe(2,end)';
    ys(101-t) = ye(2,end)';
    pause(.1);
    plot(xe(2,:)',ye(2,:)','*-');
    hold on;
    plot(xs,ys);
    hold off;
    axis([-.2 .4 0 .42]);
    %plot([min(xs) max(xs)],[0 0],'g');
    drawnow
end
```

Appendix C: Dynamic Simulation Code

```
%Vadim212.m

%Library for code uses functions from the proNEu Code Developed by ETH Zurich
%Full documentation can be found at
http://www.leggedrobotics.ethz.ch/lib/exe/fetch.php?media=research:proneu_v11_documentati
on.pdf
%Library files can be found at
%http://www.leggedrobotics.ethz.ch/doku.php?id=research:software

%% Matlab clear all
clc ;
clear ;
close all;

%% Minimal coordinates

syms qX qY qZ qAL qBE qGA real      % main body free floating
q = [qX qY qZ qAL qBE qGA]';
qDef = zeros(6,1);

syms qLH_HAA qLH_HFE qLH_KFE real   % LH (left hind) leg
q = [q',qLH_HAA qLH_HFE qLH_KFE]';
% qDef = [qDef', 0 -pi/2 0]'; %Experimenting
qDef = [qDef', pi/2 pi/2 0]'; %Works but Coords wrong

syms qRH_HAA qRH_HFE qRH_KFE real   % RH (right hind) leg
q = [q',qRH_HAA qRH_HFE qRH_KFE]';
% qDef = [qDef', pi pi/2 0]'; %Experimenting
qDef = [qDef', pi/2 -pi/2 0]'; %Works but coords wrong

%% Velocity
syms DqX DqY DqZ DqAL DqBE DqGA real % main body velocity
Dq = [DqX DqY DqZ DqAL DqBE DqGA]';


syms DqLH_HAA DqLH_HFE DqLH_KFE real
Dq = [Dq',DqLH_HAA DqLH_HFE DqLH_KFE]';
syms DqRH_HAA DqRH_HFE DqRH_KFE real
Dq = [Dq',DqRH_HAA DqRH_HFE DqRH_KFE]';
DqDef = zeros(size(Dq));


%% Parameters section start

syms mB sB ThB_xx ThB_yy ThB_zz real

% mB: mass of body
% sB: location of CG
% lB: Length of link
% ThB___ location of moment of inertia in cordinate __

%% Parameters for biped
%Order is: body, hip, ul, ll, ankle1, ankle 2

mB_Biped = [4.91589718, 0.99451015, 0.46838195, 0.72855556, 0.23602023, 0.40082228];
Cg_Biped = [0, .02945198, -.09695622, -.11278437, -0.04198568, 0.01116969];
L_Biped  = [0, 0.07778750, -0.20955000, -0.22130000, -0.01825625, -0.03016250];
Ixx_Biped= [0.11151484, 0.00283970, 0.00013197, 0.00056089, 0.00057088, 0.00206909];
Iyy_Biped= [0.04398047, 0.00199893, 0.00652038, 0.01107914, 0.00061886, 0.00233215];
Izz_Biped= [0.13005538, 0.00305081, 0.00642835, 0.01142069, 0.00083833, 0.00045364];
Leg_Offset = 0.05663311; %Offset between CG and Hip Joint Rotation

%% Theta values
%Use right hand rule off the joint to figure out which direction is
%positive
thetaL = [0 pi/4 -pi/2]; %Theta Rotations for left foot (Radians)
```

```
thetaR = [0 pi/4 -pi/2]; %Theta rotations for right foot (Radians)

%% Body Parameters
param = [mB sB ThB_xx ThB_yy ThB_zz]';
paramDef = [0.99451015 0 0.00283970 0.00199893 0.00305081]';

%% Leg Parameters
%Hip Joint
syms mH sH lH ThH_xx ThH_yy ThH_zz real
param = [param',mH sH lH ThH_xx ThH_yy ThH_zz]';
paramDef = [paramDef', mB_Biped(2), Cg_Biped(2), L_Biped(2), Ixx_Biped(2), Iyy_Biped(2),
Izz_Biped(2)]';

%Upper Leg
syms mT sT lT ThT_xx ThT_yy ThT_zz real
param = [param',mT sT lT ThT_xx ThT_yy ThT_zz]';
paramDef = [paramDef', mB_Biped(3), Cg_Biped(3), L_Biped(3), Ixx_Biped(3), Iyy_Biped(3),
Izz_Biped(3)]';

%Lower Leg
syms mS sS lS ThS_xx ThS_yy ThS_zz real
param = [param',mS sS lS ThS_xx ThS_yy ThS_zz]';
paramDef = [paramDef', mB_Biped(4), Cg_Biped(4), L_Biped(4), Ixx_Biped(4), Iyy_Biped(4),
Izz_Biped(4)]';

%Body Offsets
syms b2hx b2hy real
param = [param',b2hx b2hy]';
paramDef = [paramDef',Leg_Offset, 0]';

%Gravity
syms g real;
param = [param',g]';
paramDef = [paramDef',9.81]';

%% Torques

syms TLH_HAA TLH_HFE TLH_KFE real   % LH torques
T = [TLH_HAA TLH_HFE TLH_KFE]';
syms TRH_HAA TRH_HFE TRH_KFE real   % RH torques
T = [T', TRH_HAA TRH_HFE TRH_KFE]';

%% Gravity
% gravitational constant
I_a_grav = [0; 0; -g];

%% DYNAMICS

% Main Body
i = 1;
body(i).param.m = mB;
body(i).param.B_Th = sym(diag([ThB_xx ThB_yy ThB_zz]));
body(i).param.B_r_COG = sym([0;0;0]);
body(i).cs.P_r_PO = sym([qX;qY;qZ]);
body(i).cs.A_PB = eulerToRotMat_A_IB(qAL,qBE,qGA);
body(i).tree.parent = 0;

% Left Hip Abudction/Adduction
i = 1+1;
body(i).param.m = mH;
body(i).param.B_Th = sym(diag([ThH_xx ThH_yy ThH_zz]));
body(i).param.B_r_COG = [0;sH;0];
body(i).cs.P_r_PO = sym([-b2hx;b2hy;0]);
body(i).cs.A_PB = eulerToRotMat_A_IB(-qLH_HAA, 0, qLH_HAA+thetaL(1));
body(i).tree.parent = 1;

% Left Hip Flexion/Extension
i = i+1;
body(i).param.m = mT;
body(i).param.B_Th = sym(diag([ThT_xx ThT_yy ThT_zz]));
body(i).param.B_r_COG = [-sT;0;0];
```

```
body(i).cs.P_r_PO = sym([0;lH;0]);
body(i).cs.A_PB = eulerToRotMat_A_IB(qLH_HAA,0,0+thetaL(2));
body(i).tree.parent = i-1;

% Left Knee Flexion/Extension
i = i+1;
body(i).param.m = mS;
body(i).param.B_Th = sym(diag([ThS_xx ThS_yy ThS_zz]));
body(i).param.B_r_COG = [-sS;0;0];
body(i).cs.P_r_PO = sym([-lT;0;0]);
body(i).cs.A_PB = eulerToRotMat_A_IB(0,0,0+thetaL(3));
body(i).tree.parent = i-1;

% Left Foot
i = i+1;
body(i).param.m = 0;
body(i).param.B_Th = diag([0, 0, 0]);
body(i).param.B_r_COG = [0;0;0];
body(i).cs.P_r_PO = sym([-lS;0;0]);
body(i).cs.A_PB = eulerToRotMat_A_IB(0,0,0);
body(i).tree.parent = i-1;

% Right Hip Abudction/Adduction
i = i+1;
body(i).param.m = mH;
body(i).param.B_Th = sym(diag([ThH_xx ThH_yy ThH_zz]));
body(i).param.B_r_COG = [0;-sH;0];
body(i).cs.P_r_PO = sym([b2hx;-b2hy;0]);
body(i).cs.A_PB = eulerToRotMat_A_IB(-qLH_HAA,0,qLH_HAA+thetaR(1));
body(i).tree.parent = 1;

% Right Hip Flexion/Extension
i = i+1;
body(i).param.m = mT;
body(i).param.B_Th = sym(diag([ThT_xx ThT_yy ThT_zz]));
body(i).param.B_r_COG = [-sT;0;0];
body(i).cs.P_r_PO = sym([0;-lH;0]);
body(i).cs.A_PB = eulerToRotMat_A_IB(qLH_HAA,0,0+thetaR(2));
body(i).tree.parent = i-1;

% Right Knee Flexion/Extension
i = i+1;
body(i).param.m = mS;
body(i).param.B_Th = sym(diag([ThS_xx ThS_yy ThS_zz]));
body(i).param.B_r_COG = [-sS;0;0];
body(i).cs.P_r_PO = sym([-lT;0;0]);
body(i).cs.A_PB = eulerToRotMat_A_IB(0,0,0+thetaR(3));
body(i).tree.parent = i-1;

% Right Foot
i = i+1;
body(i).param.m = 0;
body(i).param.B_Th = diag([0, 0, 0]);
body(i).param.B_r_COG = [0;0;0];
body(i).cs.P_r_PO = sym([-lS;0;0]);
body(i).cs.A_PB = eulerToRotMat_A_IB(0,0,0);
body(i).tree.parent = i-1;

%% Force/Torque Elements

% Torque at LH hip
i = 1;
ftel(i).type = 'rot';
ftel(i).body_P = 1;
ftel(i).body_B = 2;
ftel(i).B_T = [0;0;TLH_HAA];

i = i+1;
ftel(i).type = 'rot';
ftel(i).body_P = 2;
ftel(i).body_B = 3;
```

```
ftel(i).B_T = [0;0;TLH_HFE];

i = i+1;
ftel(i).type = 'rot';
ftel(i).body_P = 3;
ftel(i).body_B = 4;
ftel(i).B_T = [0;0;TRH_KFE];

% Torque at RH hip
i = i+1;
ftel(i).type = 'rot';
ftel(i).body_P = 1;
ftel(i).body_B = 6;
ftel(i).B_T = [0;0;TRH_HAA];

i = i+1;
ftel(i).type = 'rot';
ftel(i).body_P = 6;
ftel(i).body_B = 7;
ftel(i).B_T = [0;0;TLH_HFE];

i = i+1;
ftel(i).type = 'rot';
ftel(i).body_P = 7;
ftel(i).body_B = 8;
ftel(i).B_T = [0;0;TRH_KFE];

%% Newton Euler Formulation
[sys, body, ftel] = computePNE(body,ftel,q,Dq,T,I_a_grav,param);

%% Plot Biped
plotBodies(body,param,paramDef,q,qDef);

%% Get Ground Contact Jacobians
%this would be the solution if all legs were at the ground
Js = [...
    body(5).kin.I_J_O;...
    body(9).kin.I_J_O];
```

Appendix D: Finite Element Models

Hip Joint

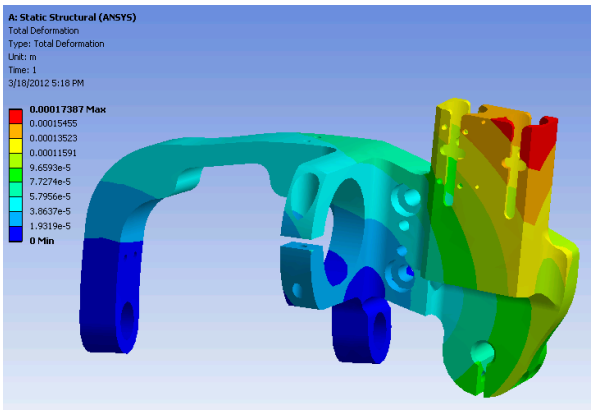

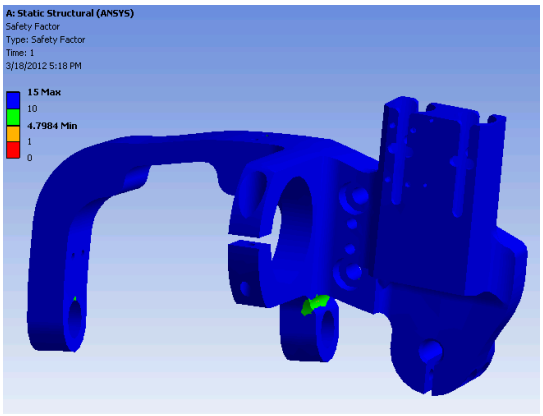

Upper Leg Joint

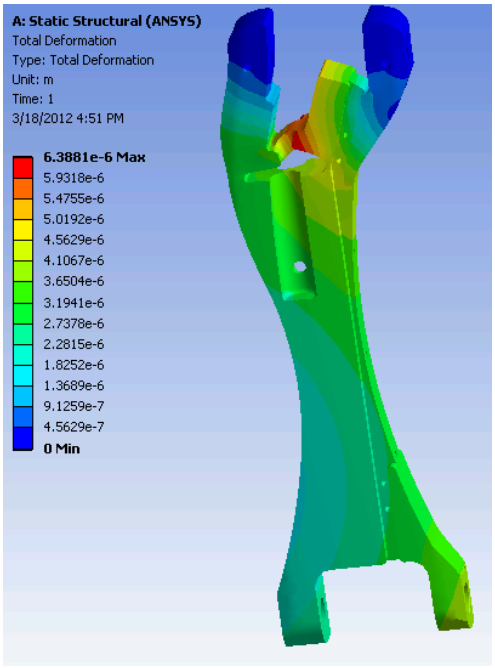

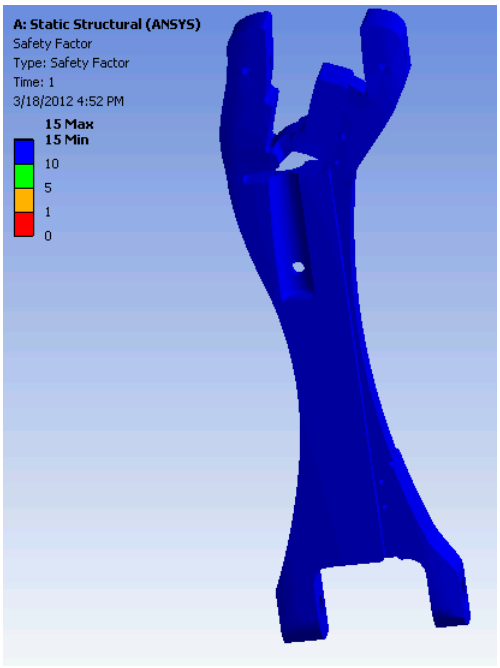

Lower Leg

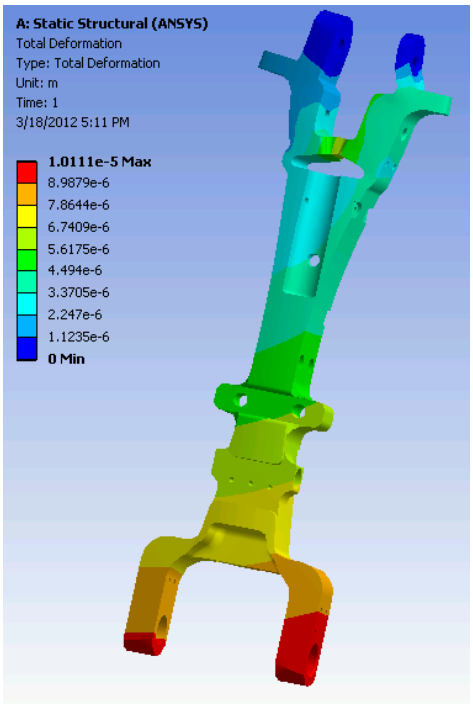

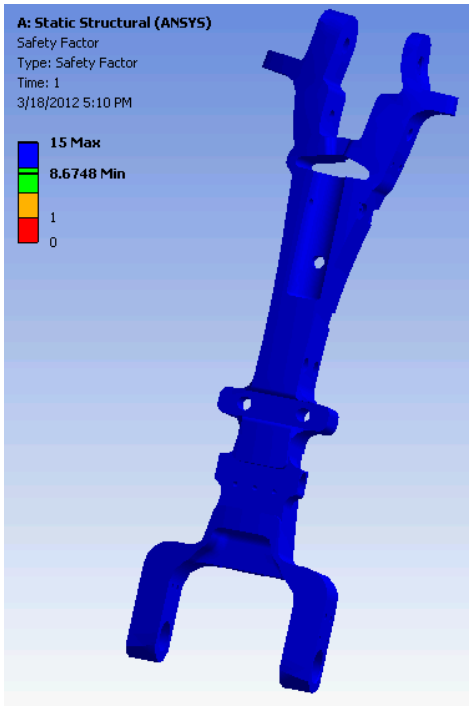

Ankle Joint

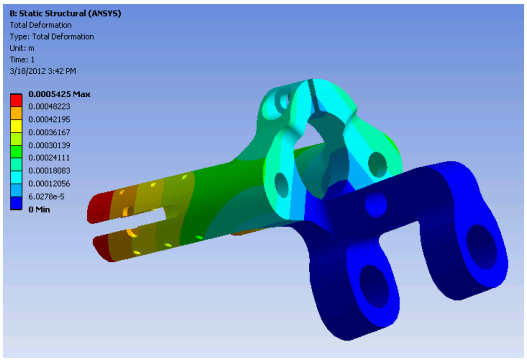

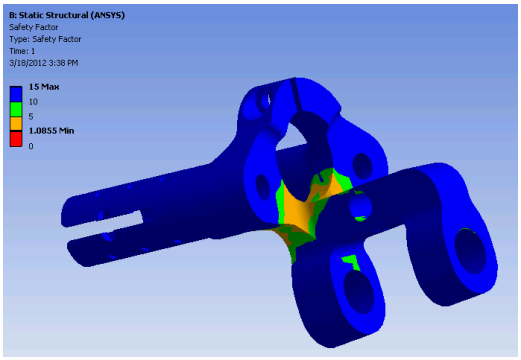

Foot Joint

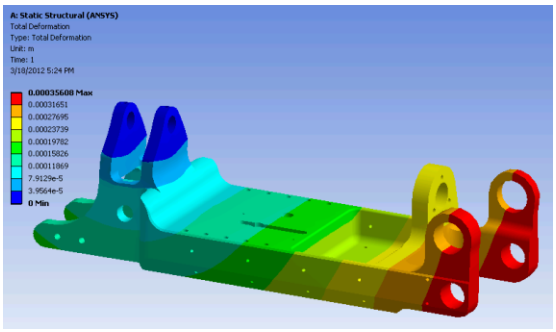

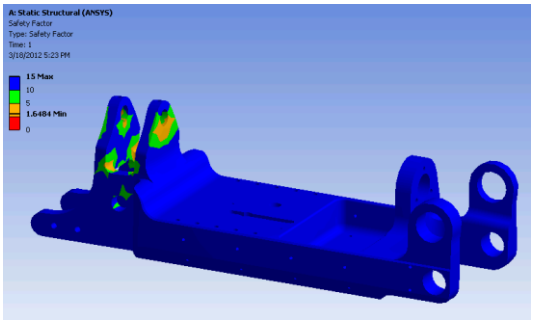

Big Toe